CORTICAL MORPHOLOGICAL CONGRUENCE AS A BIOMARKER OF BRAIN DEVELOPMENT ASSESSED WITH MAGNETIC RESONANCE IMAGING

A PREPRINT

Jacob Levman[*1,2,3,4], **Emi Takahashi**[†1,4], and **Derek Berger**[‡1]
[1]Athinoula A. Martinos Center for Biomedical Imaging, Charlestown, Massachusetts 02129
[2]Department of Computer Science, St. Francis Xavier University,Antigonish, Nova Scotia
[3]Nova Scotia Health Authority, Halifax, NS, Canada
[4]Harvard Medical School, Department of Radiology, Boston, MA, USA.

August 2, 2024

ABSTRACT

We extract a number of novel cortical morphological congruence (CMC) metrics from various anatomical cortical regions of interest (ROIs) in neurological magnetic resonance imaging (MRI) examinations. These metrics quantify the deviation of a cortical region's volume from the volume of an idealized region with the same, constant average cortical thickness and constant cross-sectional area equal to the region's cortical surface area. We examine descriptive and predictive properties of these metrics on a large (n=1113) sample of healthy subjects from the Human Connectome Project (HCP). We find a considerable consistency in CMC metrics across ROIs and subjects, suggesting a consistent proportionality relation between cortical ROI surface area, volume, and thickness. Developmental and predictive implications are discussed.

Keywords morphological · congruence · cortex · neurodevelopment · magnetic resonance imaging · healthy

1 Introduction

Characterization of human cortical development in vivo requires medical imaging technology that provides tissue contrast between gray and white matter. Magnetic resonance imaging (MRI) is sensitive to hydrogen proton concentration, which is variable across tissues, thus MRI provides excellent soft tissue contrast, including between the gray and white matter in the brain [Dubois et al., 2021]. Automated methods for extracting potential biomarkers of interest, such as a regional cortical tissue's volume, surface area (SA), or average thickness, have long been relied upon for the study of the human brain [Fischl, 2012, Levman et al., 2017, 2019a, McCann et al., 2021].

However, these volume, surface area, and thickness measurements are known to vary siginificantly aross individuals and populations [Fischl, 2012, Levman et al., 2017, 2019a], with much of this variability still to be explained. The lack of deeper understanding of the sources of variability and relationships between these measurements may potentially contribute to known reproducibility challenges in modern neuroscience studies [Martínez et al., 2015, Marek et al., 2022], and may be part of the reason that these techniques are generally not yet relied upon for clinical characterization.

Broadly, congruence is analogous to agreement between two or more objects, studies, shapes, individual measurements, etc. For instance, the results of one study may be congruent with those already in the literature, or two objects are deemed congruent if they have the same shape and size. Congruence can be applied in many ways, and has been the subject of limited and diverse studies focused on the human brain. Research has suggested that the development

[*]jlevman@stfx.ca
[†]emi@nmr.mgh.harvard.edu
[‡]dberger@stfx.ca

of visual cortical properties is dependent on visuo-proprioceptive congruence [Buisseret, 1993]. More recently, a model has been specifically developed for congruence of binocular vision (how information from the left and right eye are incorporated) in the primary visual cortex [Somaratna and Freeman, 2022]. Congruence has also been assessed between interoceptive predictions and hippocampal-related memory [Edwards-Duric et al., 2020]. Congruence between the development of the circulatory and nervous systems, or neurovascular congruence, has been the subject of a study focused on cortical development [Stubbs et al., 2009]. Additionally, it has been reported that congruence based contextual plausibility modulates cortical activity during vibrotactile perception [Kang et al., 2022]. Neuronal congruency has also been assessed in the macaque prefrontal cortex [Yao and Vanduffel, 2022]. This manuscript presents a novel set of biomarkers for characterization of regional cortical morphological congruence (CMC), which can be referred to more simply as cortical congruence (CC). The proposed methods assess the degree of congruence between multiple cortical measurements, thus providing novel biomarkers which we hypothesize may help characterize neurodevelopment.

1.1 Cortical Morphology Metrics

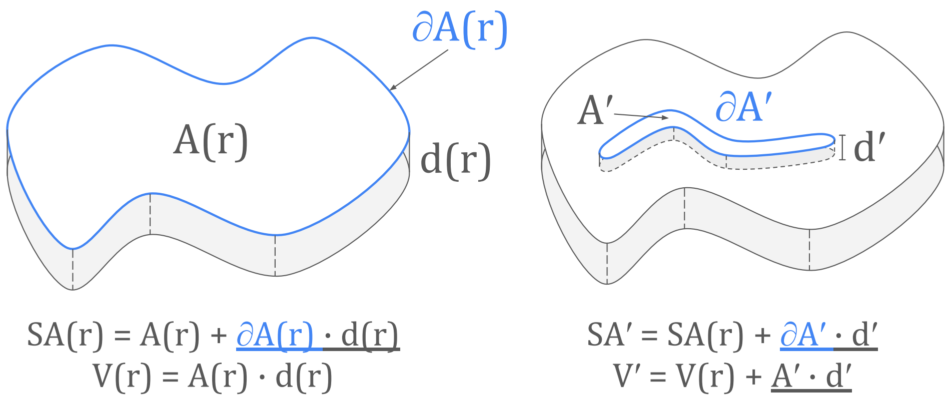

Figure 1: Left: Example idealized slab-like ROI r with constant cross-sectional area $A(r)$, surface areas $SA(r)$, thickness $d(r)$, and boundary length (perimeter) $\partial A(r)$, and thus actual volume $V(r)$ equal to $\hat{V}(r) = A(r) \cdot d(r)$. Right: example simplified deviation from slab-like ideal, with raised gyrus-like structure. An actual ROI will not, in general, have a clearly-defined perimeter, as the pial surface may curve smoothly inward to the underlying white matter, however, provided $A(r)$ is large relative to $d(r)$, then the $\partial A(r) \cdot d(r)$ term will be small, and $\hat{V}(r) = SA(r) \cdot d(r) \approx A(r) \cdot d(r) = V(r)$. Likewise, in the right figure, deviations from the ideal (e.g. gyration, of which A' is a simplified representation) means that FreeSurfer reported SA measurements will differ from those of an ideal volume on the left. However, provided $d(r)$ and d' are small relative to their respective areas, then the underlined terms above will be small.

1.1.1 Motivation

Given a cortical region of interest (ROI) r, define $V(r)$ to be the volume of that region, and $SA(r)$ and $d(r)$ to be the (outer, pial) surface area and average thickness, respectively. Then, if r has a slab- or sheet-like shape with constant cross-sectional area equal to $A(r)$, and uniform height equal to $d(r)$, then $A(r) \cdot d(r)$ is the expected volume of r (Figure 1). We thus denote the *expected-volume*, $\hat{V}(r)$, as

$$\hat{V}(r) = SA(r) \cdot \tau(r). \tag{1}$$

As most anatomical ROIs generally have a large surface area to average thickness ratio (see Table S12, for the ratios on the current data), and relatively small variance in thickness [Im et al., 2008], we expect $\hat{V}(r) \approx V(r)$, as in Figure 1. For more exotic volumes (e.g. horn-shaped, extremely non-convex, volumes with blobs joined by thin strands) or for blob-like volumes (e.g. cubelike, spherical, or regular polyhedral), the relationship between $\hat{V}(r)$ and $V(r)$ (and indeed the values of $d(r)$ itself) lacks interpretability. However, for regions that are more sheet-like (or which resemble a crumpled sheet), we expect $\hat{V}(r)$ to better approximate $V(r)$. Thus, for cortical ROIs, we expect greater dissimilarity between $\hat{V}(r)$ and $V(r)$ to index the complexity of the shape of r.

1.1.2 Base Metrics

We wish to define metrics relating $\hat{V}$ and V for an ROI r. The more an ROI r resembles or is congruent to a shape like in Figure 1—i.e. has limited curvature, regular thickness, and small average thickness relative to the surface area—then the closer $\hat{V}(r)$ will be to $V(r)$. By contrast, incongruence between $\hat{V}(r)$ and $V(r)$ will increase for ROIs which are more blob-like (i.e. have large $\tau(r)$ relative to SA), or may increase for ROIs which have more variable thickness and/or curvature (e.g. any ROI with convoluted and/or tube-like structures, have higher overall curvature, or are more gyrated or sulcated).

We thus define the *cortical morphological congruence*[4], CMC, to be:

$$\text{CMC}(r) = \frac{V(r)}{\hat{V}(r)}. \tag{2}$$

As cortical ROIs manifest in both hemispheres, we more precisely define the *left* and *right* CMC as:

$$\text{CMC}_\ell = \text{CMC}_{\text{Lateral}}(r_\ell) \tag{3}$$
$$\text{CMC}_r = \text{CMC}_{\text{Lateral}}(r_r). \tag{4}$$

We also define the *bilateral* CMC, for ROI r with left and right hemisphere volumes r_l and r_r, respectively, as:

$$\text{CMC}_{lr} = \frac{V(r_\ell) + V(r_r)}{\hat{V}(r_\ell) + \hat{V}(r_r)} = \frac{V_\ell(r) + V_r(r)}{\hat{V}_\ell(r) + \hat{V}_r(r)} = \frac{\text{ROI total volume}}{\text{ROI total expected volume}}. \tag{5}$$

1.1.3 Asymmetry Metrics

Define the *asymmetric* CMC metrics:

$$\text{CMC}_{l-r} = \text{CMC}_l - \text{CMC}_r \tag{6}$$

and

$$\text{CMC}_{|l-r|} = |\text{CMC}_{l-r}| \tag{7}$$

to be the *asymmetric CMC differences*, with Equation 6 and Equation 7 defining the *signed* and *unsigned* CMC asymmetric differences, respectively. Also define

$$\text{CMC}_{l/r} = \text{CMC}_l / \text{CMC}_r \tag{8}$$

to be the *asymmetric CMC ratio*. In addition, the expected volume can be computed unilaterally

$$\hat{V}(r_\ell) = \hat{V}_\ell(r) = SA(r_\ell) \cdot \tau(r_\ell) \tag{9}$$
$$\hat{V}(r_r) = \hat{V}_r(r) = SA(r_r) \cdot \tau(r_r) \tag{10}$$

or bilaterally

$$\hat{V}_{\ell r}(r) = \hat{V}(r_{\ell r}) = \hat{V}_\ell(r) + \hat{V}_r(r). \tag{11}$$

This yields a variety of CMC-related metrics to assess, depending on the hemispheres of interest, and outlined in Table 1.

All CMC metrics index aspects of a cortical region's shape. In the case of equality of $\hat{V}(r)$ and $V(r)$, this produces a CMC metric value of 0 or 1. Deviations from these values in either direction may have implications for structural cortical presentation and neurological development (see Discussion).

[4]The motivation for the terminology being *congruence to simple* (i.e. sheet-like) *structure*, and the term 'congruence' chosen since when $V(r) \approx \hat{V}(r)$, it suggests $SA(r) \approx A(r)$ and $\tau(r) \approx d(r)$, i.e. the shapes measurements are approximately equal.

CMC Metric Class	Can be computed for hemisphere: left	right	both	Asym	n
$\hat{V}$	$\hat{V}_\ell$	$\hat{V}_r$	$\hat{V}_{\ell r}$	×	102
CMC	CMC_ℓ	CMC_r	$\text{CMC}_{\ell r}$	×	102
$\text{CMC}_{\ell-r}$	×	×	$\text{CMC}_{\ell-r}$	✓	34
$\text{CMC}_{\lvert\ell-r\rvert}$	×	×	$\text{CMC}_{\lvert\ell-r\rvert}$	✓	34
$\text{CMC}_{\ell/r}$	×	×	$\text{CMC}_{\ell/r}$	✓	34

Table 1: CMC feature classes and variants. Asym = metric assesses CMC asymmetry; n = number of distinct features per subject (34 for each ROI hemisphere, including bilateral metric variants.)

2 Methods

2.1 Subject Populations and Imaging

Data were provided in part by the Human Connectome Project, WU-Minn Consortium (Principal Investigators: David Van Essen and Kamil Ugurbil; 1U54MH091657) funded by the 16 NIH Institutes and Centers that support the NIH Blueprint for Neuroscience Research; and by the McDonnell Center for Systems Neuroscience at Washington University. This cohort included 1,113 healthy subjects imaged with MRI. Detailed information on the magnetic resonance imaging (MRI) scanners and protocols used in the Human Connectome Project dataset are available in the literature [Elam et al., 2021].

2.2 Postprocessing

The Human Connectome Project's WU-Minn HCP cohort (n=1,113 with MRI examinations) was processed by FreeSurfer [Fischl, 2012] and the results were made publicly available through the Human Connectome Project's website. Notably, the cortex is parcellated into the 34 anatomical ROIs defined in Desikan et al. [2006], and corresponding ROI geometric statistics are available for each ROI.

2.3 Features for Predictive Analysis

For each of the 34 cortical ROIs, all CMC measurements were computed for each subject. These were computed from the base FreeSurfer cortical measurements available in the HCP data. That is the FreeSurfer "ThickAvg", "GrayVol", and "SurfArea" measurements were used for $\tau(r)$, $V(r)$, and $SA(r)$, respectively. Descriptive statistics of both the base FreeSurfer and extracted features are shown in Table 2. Dispersion coefficients are included to better facilitate comparison of the feature scales.

ROI Statistic Feature	μ	σ	CD	rCD
CMC	1.142	0.026	0.023	0.015
$\text{CMC}_{\ell/r}$	1.000	0.026	0.026	0.017
$\text{CMC}_{\ell-r}$	-0.000	0.029	3.143	2.060
$\text{CMC}_{\lvert\ell-r\rvert}$	0.026	0.020	0.772	0.567
$\hat{V}$	7582.320	2947.661	0.386	0.315
V	8505.020	3307.624	0.386	0.315
SA	2129.731	306.353	0.151	0.103
τ	2.698	0.129	0.048	0.031

Table 2: Median descriptive statistics of features used in predictive models, summarizing across all ROIs and hemispheres (left, right, and both hemispheres for non-asymmetry CMC metrics). n = number of ROI statistics summarized (1113 subjects × 34 ROIs = 37 842); CD = coefficient of dispersion / variation, e.g. σ/μ; rCD = robust / quartile coefficient of dispersion [Bonett, 2006].

Behavioural data initial shape
↓
(1206, 582)
↓
Remove junk features
↓
(1206, 400)
↓
Remove highly-correlated
↓
(1206, 375)
↓
Remove constant features
↓
(1206, 369)
↓
Remove subjects with all missing value
↓
(1113, 369)
↓
Remove sex and age class as target features
↓
(1113, 367)

Figure 2: Junk features include, book-keeping (IDs, scan counts) and subscale items, or features with 200 or more NaN values. Highly-correlated features include e.g. pairs like `dexterity_unadj` and `dexterity_ageadj`, with correlations above 0.95, and other features with correlations of 1.0.

2.4 Statistical and Predictive Analyses

For each of the 34 cortical regions r available from the FreeSurfer analysis (see Table 7), all CMC features are computed for each subject. Then, we run run various statistical and predictive analyses based on these extracted features.

2.4.1 Descriptive Statistics

For each CMC feature and ROI, we compute descriptive measures of group separation by sex using Cohen's d and the Mann-Whitney U test. We also compare CMC_l and CMC_r in a similar manner, to asses if there are differences in the CMC by hemisphere. We also compute Spearman correlations with subject age for all features. Spearman correlation is preferred as only age bins are available in the HCP phenotypic data.

2.4.2 Predictive Analyses

The HCP data provides a wealth of openly-accessible behavioural data on participating subjects. Full details of the hundreds of features are available online.

Behavioural Targets To investigate the predictive potential of CMC features, a number of *ad hoc* regression targets were extracted from the HCP behavioural data. First, behavioural data were cleaned of irrelevant, missing, constant, or redundant features (see Section 2.4.2). Then, the remaining behavioural features were reduced in an exploratory fashion.

First, clustering was performed on the features using HDBSCAN [Campello et al., 2015, Pedregosa et al., 2011] with the absolute value of the Pearson correlation as the feature distance metric. HDBSCAN does not require specifying the number of clusters, and allows for assignment to "noise" or "background" clusters, and thus acts as a natural method to

target	task	component(s)
gambling_perf	gambling	performance
emotion_perf	emotion processing	performance
language_rt	language processing	reaction time
relational_rt	relational processing	reaction time
emotion_rt	emotion processing	reaction time
language_perf	language	reaction time
p_matrices	progressive matrices	performance
social_rt	social cognition	reaction time
psqi_latent	Pittsburg Sleep Quality Index factor [Buysse et al., 1989]	score
gambling_rt	gambling task	reaction time
social_random_perf	social cognition (random blocks)	performance
int_g_like	general intelligence	see Table A 24
neg_emotionality	negative emotionality	see Table A 25
wm_rt	working memory (n-back)	reaction time
wm_perf	working memory	performance

Table 3: Brief descriptions of factor targets.

notice patterns of correlation in the data. That is, by pooling together all features and ignoring the feature measurement procedures, we can find natural clusters of measurements without assuming that items are correlated simply by virtue of being members of the same behavioural test or measurement instrument.

Second, after interpolating missing values with the feature means, HDBSCAN feature clusters were reduced to a single dimension via exploratory factor analysis. Factor analysis is a linear dimensionality reduction method wherein the reduced factor can be interpreted as a latent variable that well-describes the unreduced data, accounting for noise [Cattell, 1978, Child, 2006]. Factor analysis was chosen here over PCA as the reduced unidimensional feature is more readily interpreted as a latent variable free from error variance Attias [1999].

The resulting factor target names, clusters and loadings are shown in Appendix B, as are brief descriptions in Table 3. Most of the clusters appear to have face value, suggesting a useful clustering by HDBSCAN. For example, the factor we have labeled "int_g_like" involves a number of features measuring fluid and crystalized intelligence, processing speed, and performance at various sorting and reading tasks (Table S24), and so might be interpreted broadly as a general intelligence factor.

In the interest of space, and since many factor targets turn out not to be predictable at all, we refrain from describing each of the extracted factor targets here, and relegate such explanation to the discussion. Ultimately, the factors are defined by the loadings of their respective items: these are listed in Appendix B. Likewise, the battery of behavioural tasks administered to HCP subjects is too extensive to detail here: the interested reader is referred to Barch et al. [2013].

FreeSurfer Comparisons As CMC features are derived from features extracted from FreeSurfer (FS) cortical analyses, we compare model predictions on feature sets that: include only FS features, include only CMC features, and include both FS and CMC features.

Automated Machine Learning via `df-analyze` Predictive analyses were completed with `df-analyze`, publicly available software, developed in house to automate data cleaning and preprocessing, and the subsequent feature selection, fitting, tuning, and validation of various classic machine-learning (ML) models from scikit-learn [Pedregosa et al., 2011], LightGBM [Ke et al., 2017] , and PyTorch [Ansel et al., 2024]. The software was previously applied to brain MRI predictive application focused on schizophrenia diagnostics [Levman et al., 2022], and automates the search for an optimal combination of feature selection, models, and hyperparameters on simple tabular data.

In the current work, `df-analyze` is used to compare all combinations of the following:

- feature sets (FS only, CMC only, and FS and CMC features)
- regression models (ElasticNet [Zou and Hastie, 2005, Pedregosa et al., 2011], LightGBM [Ke et al., 2017], and dummy regressors [Pedregosa et al., 2011])
- feature selection methods
  - no selection (all features are used for predictions)
  - stepwise (forward stepwise selection with a linear model)

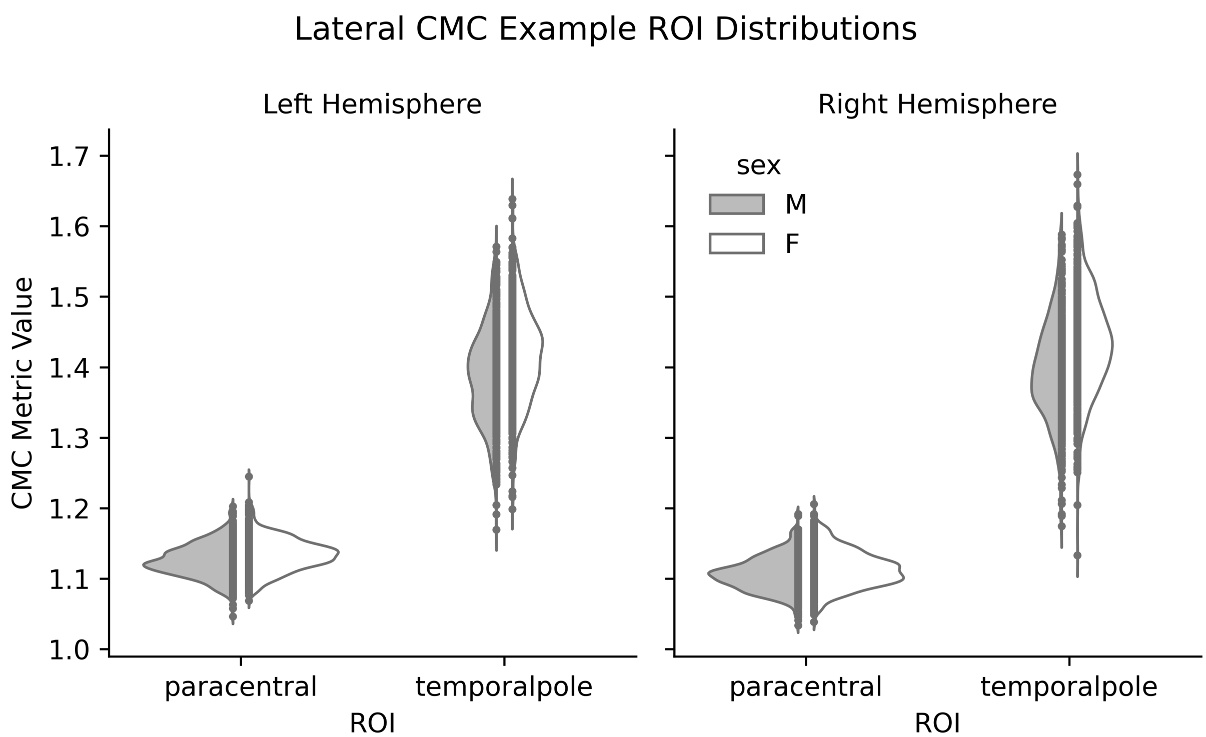

Figure 3: Example distributions of CMC features for two ROIs. The temporal pole has the largest CMC separation by sex (see Table 5; Cohen's $|d| = 0.50$), and relatively large standard deviations compared to other ROIs. The paracentral lobule, by contrast, has a typical standard deviation for CMC metrics, but the largest differences between hemispheres (Cohen's $|d| = 0.80$).

  - embedded methods (feature importances from ElasticNet and LightGBM)
  - two filter methods:
    1. mutual information of each univariate feature with respect to the factor target
    2. predictive accuracy of each univariate feature with respect to the factor target
- factor targets (see [Appendix B](appendix-b))

As all factor targets are continuous variables, we use R^2, the coefficient of determination, and the mean absolute error (MAE) to assess model fit. For any combination of feature set, feature selection method, and target, a dummy regression model (which predicts either the target mean or median, whichever results in better cross-validated performance) is fit, with the intention that prediction performance of other models is considered meaningful only if both $R^2 > 0$ and the the non-dummy model has a lower MAE than the dummy model.

All models are hyperparameter-tuned with Optuna [Akiba et al., 2019], using a tuning budget of 100 trials and 5-fold cross-validation for evaluation. All tuning, and feature selection is done on a separate training data split using 50% of the available samples, with final results reported on the remaining 50%, to ensure there is no double-dipping or data leakage during these steps.

All source code used for the analyses in this study is available online [DM-Berger, 2024].

3 Results

3.1 Descriptive Statistics

3.1.1 CMC Features by Sex

While all base FreeSurfer features differ significantly by sex, as do the base CMC features and expected volume features, $\text{CMC}_{\ell/r}$ and $\text{CMC}_{\ell-r}$ differ only marginally (Table 4).

	d				p	
Feature	μ	σ	min	max	min	max
CMC	-0.13	0.19	-0.53	0.28	0.00	1.00
$CMC_{\ell/r}$	0.01	0.08	-0.13	0.21	0.04	1.00
$CMC_{\ell-r}$	0.01	0.08	-0.13	0.20	0.04	1.00
$CMC_{\lvert\ell-r\rvert}$	-0.02	0.09	-0.24	0.13	0.39	1.00
$\hat{V}$	0.34	0.05	0.18	0.43	0.00	0.00
V	0.33	0.06	0.12	0.43	0.00	0.00
SA	0.89	0.22	0.49	1.23	0.00	0.00
τ	0.07	0.13	-0.12	0.52	0.00	1.00

Table 4: Summary of Cohen's d values for sex, for each ROI. I.e. each row summarizes 34 Cohen's d values, one for each ROI, and where each d value summarizes 1 113 subjects (M=507, F=606) × the number of ROI hemispheres (1 or 3 for asymmetry and non-asymmetry measures). Rightmost columns show the smallest and largest of the 34 p-values associated with the Mann-Whitney U statistic. All p-values are corrected for multiple comparisons by the Holm-Bonferroni step-down method.

The base CMC features differing significantly by sex are shown in Table 5. Note that the minimum or maximum Cohen's d values shown in Table 4 need not represent a significant group difference, and thus the largest observed CMC separation by sex is in the temporal poles overall (first row of Table 5), with this separation being larger in the left hemisphere (second row) than in the right (fourth row).

ROI	d	U	U (p)
bh-temporalpole	-0.294	127593.000	0.000
lh-temporalpole	-0.283	129332.000	0.000
bh-insula	0.233	174258.000	0.004
rh-temporalpole	-0.229	134217.000	0.010
bh-paracentral	-0.187	136173.000	0.035
rh-paracentral	-0.177	136298.000	0.039

Table 5: CMC features with significant separation by sex. d = Cohen's d, with positive sign indicating larger metric values for males; U = Mann-Whitney U, U (p) = p-value for Mann-Whitney U. bh = bilateral (both hemispheres) CMC metric; lh/rh = left/right hemisphere lateral CMC metric Note: p-values are adjusted for multiple comparisons using the Holm-Bonferroni stepdown method.

3.1.2 CMC Features by Laterality, Age, and Sex

Excluding the asymmetry CMC measures, we find significant differences for all feature classes (Table 6). For the base CMC metrics, only the superior frontal and pars opercularis regions do not differ significantly by hemisphere (Table 7).

Feature	μ	σ	min	max	n_sig
CMC	-0.12	0.18	-0.50	0.27	32
$\hat{V}$	0.89	0.23	0.47	1.33	31
V	0.86	0.25	0.30	1.37	29
SA	0.89	0.22	0.46	1.23	28
τ	0.07	0.13	-0.12	0.53	32

Table 6: Summary of Cohen's d values for left vs. right CMC differences, for each ROI. I.e. each row summarizes 34 Cohen's d values, one for each ROI, and where each d value summarizes 1 113 subjects. n_sig = amount of the 34 (adjusted) p-values < 0.05.

Significant feature-age correlations are shown in Table 8. Note that, when restricting to a specific sex, the feature-age correlations tend not to be significant (r_{M_p} and r_{F_p} columns), which may reflect the reduced sample size when restricting to one sex.

ROI	d	W	p
inferiortemporal	-1.890	0.000	0.000
insula	-1.778	21.000	0.000
pericalcarine	-1.883	0.000	0.000
precuneus	-1.772	0.000	0.000
precentral	-1.661	75.000	0.000
rostralanteriorcingulate	1.673	143.000	0.000
fusiform	1.706	260.000	0.000
superiorparietal	-1.598	376.000	0.000
postcentral	1.625	534.000	0.000
paracentral	-1.406	593.000	0.000
caudalanteriorcingulate	1.630	1092.000	0.000
lateralorbitofrontal	-1.337	1710.000	0.000
isthmuscingulate	-1.498	1886.000	0.000
cuneus	-1.648	2429.000	0.000
transversetemporal	-1.510	2995.000	0.000
lingual	1.531	5488.000	0.000
posteriorcingulate	1.375	8640.000	0.000
superiortemporal	1.176	18322.000	0.000
parahippocampal	-0.934	39694.000	0.000
middletemporal	0.940	44794.000	0.000
supramarginal	1.019	59895.000	0.000
frontalpole	0.880	70533.000	0.000
parsorbitalis	-0.939	76597.000	0.000
lateraloccipital	0.894	79894.000	0.000
parstriangularis	0.611	90160.000	0.000
caudalmiddlefrontal	0.589	127030.000	0.000
inferiorparietal	0.482	171122.000	0.000
medialorbitofrontal	-0.357	180895.000	0.000
bankssts	-0.417	187242.000	0.000
entorhinal	-0.364	192057.000	0.000
rostralmiddlefrontal	0.275	224623.000	0.000
temporalpole	-0.216	235096.000	0.000
parsopercularis	-0.055	298155.000	0.541
superiorfrontal	0.030	306615.000	0.754

Table 7: Measures of separation of lateral CMC features (left vs. right hemisphere). d = Cohen's d, with a positive sign indicating greater congruence in left hemisphere ROIs; W = Wilcoxon signed rank test; p = p-value for W; Note: p-values are adjusted for multiple comparisons using the Holm-Bonferroni stepdown method

3.2 Predictive Analyses

3.2.1 Predictive Performance

For the factor targets `emotion_perf`, `neg_emotionality`, `psqi_latent`, `relational_rt`, and `social_random_perf`, no models exceeded the performance of the dummy regressors, implying that neither FreeSurfer nor CMC features had predictive utility for these targets.

Note that, as `df-analyze` is exhaustive in its search for optimal models, a large number of highly-misspecified models (i.e. with performance failing to exceed dummy peformance) can be produced. Including such "trivial" models can be misleading in summaries (for example, if most feature selection methods perform poorly, but a single selection method has excellent performance). Thus, we limit summaries and tables to description of "non-trivial" models exceeding dummy performance. Readers interested in complete tables should refer to Appendix C, Table 27.

Table 9 summarizes the proportions of non-trivial models for each target and feature source. Thus, for example, models predicting `int_g_like` are all non-trivial when using only CMC features or when using only FreeSurfer features, but less than half exceed dummy performance when both CMC and FreeSurfer features are used in combination.

Table 10 summarizes the absolute best model performances for each combination of target and feature source. That is, for the `int_g_like` target, the best performance ($R^2 = 0.144$) results from using only FreeSurfer features. Note,

ROI	CMC class	r	r_p	r_M	r_{M_p}	r_F	r_{F_p}	$p_{\min}$
bh-superiorfrontal	$\text{CMC}_{\ell r}$	-0.1795	0.0000	-0.1870	0.0198	-0.1909	0.0020	0.0000
bh-caudalmiddlefrontal	$\text{CMC}_{\ell r}$	-0.1778	0.0000	-0.1848	0.0249	-0.1649	0.0389	0.0000
lh-middletemporal	$\hat{V}_\ell$	-0.1709	0.0000	-0.0418	1.0000	-0.1476	0.2224	0.0000
bh-isthmuscingulate	$\hat{V}_{\ell r}$	-0.1675	0.0000	-0.0902	1.0000	-0.0870	1.0000	0.0000
bh-middletemporal	$\hat{V}_{\ell r}$	-0.1667	0.0000	-0.0429	1.0000	-0.1312	0.9631	0.0000
lh-isthmuscingulate	$\hat{V}_\ell$	-0.1656	0.0000	-0.0960	1.0000	-0.0799	1.0000	0.0000
lh-lateralorbitofrontal	CMC_ℓ	-0.1652	0.0000	-0.1757	0.0602	-0.1382	0.5262	0.0000
bh-lateralorbitofrontal	$\hat{V}_{\ell r}$	-0.1651	0.0000	0.0139	1.0000	-0.1747	0.0134	0.0000
rh-lateralorbitofrontal	$\hat{V}_r$	-0.1635	0.0000	0.0313	1.0000	-0.1924	0.0016	0.0000
rh-superiorfrontal	CMC_r	-0.1626	0.0000	-0.1755	0.0609	-0.1649	0.0391	0.0000
bh-postcentral	$\hat{V}_{\ell r}$	-0.1611	0.0001	-0.0072	1.0000	-0.1353	0.6805	0.0001
rh-inferiorparietal	$\hat{V}_r$	-0.1574	0.0001	-0.0610	1.0000	-0.1198	1.0000	0.0001
rh-postcentral	$\hat{V}_r$	-0.1548	0.0002	-0.0199	1.0000	-0.1181	1.0000	0.0002
bh-lateralorbitofrontal	$\text{CMC}_{\ell r}$	-0.1542	0.0002	-0.1637	0.1791	-0.1306	1.0000	0.0002
bh-rostralmiddlefrontal	$\hat{V}_{\ell r}$	-0.1534	0.0002	0.0151	1.0000	-0.1530	0.1321	0.0002
bh-inferiorparietal	$\hat{V}_{\ell r}$	-0.1531	0.0003	-0.0526	1.0000	-0.1024	1.0000	0.0003
lh-superiorfrontal	CMC_ℓ	-0.1476	0.0007	-0.1489	0.6230	-0.1585	0.0761	0.0007
lh-postcentral	$\hat{V}_\ell$	-0.1475	0.0007	0.0114	1.0000	-0.1421	0.3679	0.0007
rh-caudalmiddlefrontal	CMC_r	-0.1467	0.0008	-0.1574	0.3076	-0.1451	0.2807	0.0008
lh-lateralorbitofrontal	$\hat{V}_\ell$	-0.1460	0.0009	-0.0012	1.0000	-0.1333	0.8081	0.0009
rh-middletemporal	$\hat{V}_r$	-0.1455	0.0010	-0.0368	1.0000	-0.1070	1.0000	0.0010
rh-rostralmiddlefrontal	$\hat{V}_r$	-0.1438	0.0013	0.0228	1.0000	-0.1489	0.1977	0.0013
bh-inferiortemporal	$\hat{V}_{\ell r}$	-0.1433	0.0014	-0.0436	1.0000	-0.0866	1.0000	0.0014
lh-caudalmiddlefrontal	CMC_ℓ	-0.1406	0.0022	-0.1354	1.0000	-0.1313	0.9563	0.0022
lh-inferiortemporal	$\hat{V}_\ell$	-0.1398	0.0025	-0.0372	1.0000	-0.0951	1.0000	0.0025
bh-fusiform	$\hat{V}_{\ell r}$	-0.1391	0.0028	-0.0177	1.0000	-0.0807	1.0000	0.0028
lh-fusiform	$\hat{V}_\ell$	-0.1386	0.0031	-0.0473	1.0000	-0.0780	1.0000	0.0031
bh-superiorparietal	$\hat{V}_{\ell r}$	-0.1354	0.0051	-0.0110	1.0000	-0.1461	0.2545	0.0051
rh-isthmuscingulate	$\hat{V}_r$	-0.1347	0.0058	-0.0322	1.0000	-0.0956	1.0000	0.0058
rh-superiorfrontal	$\hat{V}_r$	-0.1343	0.0061	-0.0112	1.0000	-0.0915	1.0000	0.0061
lh-rostralmiddlefrontal	$\hat{V}_\ell$	-0.1334	0.0070	0.0071	1.0000	-0.1302	1.0000	0.0070
bh-superiortemporal	$\hat{V}_{\ell r}$	-0.1334	0.0071	-0.0164	1.0000	-0.0794	1.0000	0.0071
bh-superiorfrontal	$\hat{V}_{\ell r}$	-0.1317	0.0092	0.0030	1.0000	-0.0904	1.0000	0.0092
rh-superiorparietal	$\hat{V}_r$	-0.1304	0.0113	-0.0136	1.0000	-0.1196	1.0000	0.0113
bh-frontalpole	$\hat{V}_{\ell r}$	-0.1296	0.0127	-0.0467	1.0000	-0.1093	1.0000	0.0127
bh-precentral	$\text{CMC}_{\ell r}$	-0.1292	0.0135	-0.1227	1.0000	-0.1452	0.2787	0.0135
rh-superiortemporal	$\hat{V}_r$	-0.1289	0.0141	-0.0312	1.0000	-0.0820	1.0000	0.0141
bh-parstriangularis	$\hat{V}_{\ell r}$	-0.1287	0.0146	-0.0280	1.0000	-0.0761	1.0000	0.0146
bh-rostralmiddlefrontal	$\text{CMC}_{\ell r}$	-0.1253	0.0242	-0.1491	0.6121	-0.0928	1.0000	0.0242
rh-posteriorcingulate	$\hat{V}_r$	-0.1248	0.0259	-0.0042	1.0000	-0.1350	0.6939	0.0259
rh-parstriangularis	CMC_r	-0.1068	0.2954	-0.1839	0.0271	-0.0426	1.0000	0.0271
bh-precentral	$\hat{V}_{\ell r}$	-0.1242	0.0282	0.0236	1.0000	-0.0647	1.0000	0.0282
lh-posteriorcingulate	CMC_ℓ	-0.1241	0.0286	-0.1145	1.0000	-0.1163	1.0000	0.0286
lh-parsopercularis	$\hat{V}_\ell$	-0.1238	0.0300	-0.0737	1.0000	-0.0705	1.0000	0.0300
bh-precuneus	$\hat{V}_{\ell r}$	-0.1237	0.0304	-0.0031	1.0000	-0.1123	1.0000	0.0304
rh-parstriangularis	$\hat{V}_r$	-0.1226	0.0357	-0.0316	1.0000	-0.0848	1.0000	0.0357
bh-frontalpole	$\text{CMC}_{\ell r}$	-0.1223	0.0370	-0.0943	1.0000	-0.1600	0.0655	0.0370
rh-frontalpole	$\hat{V}_r$	-0.1223	0.0373	-0.0728	1.0000	-0.0873	1.0000	0.0373
bh-parsopercularis	$\hat{V}_{\ell r}$	-0.1223	0.0373	-0.0648	1.0000	-0.0699	1.0000	0.0373
rh-precuneus	$\hat{V}_r$	-0.1214	0.0423	-0.0022	1.0000	-0.0939	1.0000	0.0423

Table 8: Spearman correlations between CMC feature classes, age, and sex. r = Spearman's correlation with age, all subjects; r_X = male/female correlation for X = M/F, respectively; $[]_p$ = two-sided p-value for metric []; $p_{\min}$ = smallest p-value of each row; Note: All p-values are adjusted for multiple comparisons using the Holm-Bonferroni stepdown method

however, that the differences in the MAE among these best models are quite small, and, practically, there is likely similar predictive information in both FreeSurfer and CMC metrics overall. Note also that the inclusion of *both* FreeSurfer and CMC features in a model generally has a negative impact on peak model performance.

target	source	
emotion_rt	FS	0.583
emotion_rt	CMC	0.417
emotion_rt	FS+CMC	0.292
gambling_perf	FS	0.167
gambling_perf	CMC	0.083
gambling_rt	CMC	0.500
gambling_rt	FS	0.333
gambling_rt	FS+CMC	0.208
int_g_like	CMC	1.000
int_g_like	FS	1.000
int_g_like	FS+CMC	0.458
language_perf	CMC	0.667
language_perf	FS	0.667
language_perf	FS+CMC	0.292
language_rt	FS	0.083
p_matrices	FS	0.583
p_matrices	CMC	0.167
p_matrices	FS+CMC	0.167
social_rt	FS	0.167
wm_perf	FS	0.250
wm_perf	CMC	0.167
wm_rt	CMC	0.250
wm_rt	FS	0.083
wm_rt	FS+CMC	0.083

Table 9: For each combination of target and feature class, the proportion of model runs that exceeds dummy performance. Omitted combinations have no runs exceeding dummy performance. source = feature source: FS = FreeSurfer features only, CMC = CMC features only, FS+CMC = both FS and CMC features.

target	feats	selection	model	r2	mae	mae+
emotion_rt	FS	none	lgbm	0.046	0.190	0.004
emotion_rt	FS+CMC	none	lgbm	0.044	0.190	0.003
emotion_rt	CMC	wrap	elastic	0.032	0.191	0.003
gambling_perf	CMC	wrap	elastic	0.003	0.165	0.001
gambling_perf	FS	embed_linear	lgbm	0.001	0.166	0.000
gambling_rt	FS+CMC	pred	lgbm	0.021	0.200	0.006
gambling_rt	FS	embed_linear	lgbm	0.014	0.203	0.003
gambling_rt	CMC	wrap	elastic	0.015	0.203	0.003
int_g_like	FS	none	elastic	0.144	0.184	0.018
int_g_like	CMC	embed_lgbm	elastic	0.104	0.191	0.011
int_g_like	FS+CMC	pred	elastic	0.076	0.191	0.011
language_perf	FS	embed_linear	lgbm	0.106	0.194	0.010
language_perf	CMC	assoc	lgbm	0.093	0.196	0.007
language_perf	FS+CMC	assoc	lgbm	0.089	0.197	0.007
language_rt	FS	wrap	lgbm	0.002	0.190	0.000
p_matrices	CMC	wrap	elastic	0.033	0.234	0.004
p_matrices	FS	pred	lgbm	0.030	0.235	0.003
p_matrices	FS+CMC	wrap	elastic	0.035	0.235	0.003
social_rt	FS	embed_lgbm	lgbm	0.001	0.194	0.000
wm_perf	FS	embed_lgbm	lgbm	0.097	0.196	0.003
wm_perf	CMC	embed_linear	lgbm	0.093	0.197	0.002
wm_rt	CMC	pred	lgbm	0.025	0.195	0.002
wm_rt	FS	none	lgbm	0.021	0.195	0.002
wm_rt	FS+CMC	wrap	elastic	0.006	0.196	0.001

Table 10: Best model performance, for each combination of target and feature source. Missing combinations indicate no runs in that combination exceed dummy model performance. source = feature source: FS = FreeSurfer features only, CMC = CMC features only, FS+CMC = both FS and CMC features. selection = feature selection method: wrap = stepwise selection with linear model wrapper; pred = univariate prediction; embed_[x] = embedded selection with model [x]; none = all features used in model. model = regressor model: lgbm = LightGBM; elastic = ElasticNet. r2 = coefficient of determination; mae = mean absolute error; mae+ = improvement in MAE relative to dummy model MAE.

3.2.2 Selected Features

A number of model runs involve both FS and CMC feature sets. As `df-analyze` automates simple feature selection via filter, wrapper, and embedded methods, it is possible to roughly examine the proportion of CMC features selected by some of the most predictive models. These are shown below in Table 11.

Note that performances are lower than in Table 10, as the best performing models usually did not use a mixed feature set (e.g. "FS+CMC"), or occured in models where no feature selection was performend, and thus do not allow assessing the relative contribution of the different features.

4 Discussion

The human brain's regional cortical development proceeds with a variety of underlying factors maturing in tandem with one another. Cortical volume, surface area and thickness are excellent examples of measurable biomarkers that

target	selection	model	r2	mae	mae+	p_sel_cmc	p_sel_feat_cmc
int_g_like	assoc	lgbm	0.110	0.193	0.009	1.000	0.504
int_g_like	assoc	elastic	0.072	0.192	0.010	1.000	0.504
p_matrices	assoc	lgbm	0.015	0.237	0.002	1.000	0.504
wm_rt	assoc	lgbm	0.016	0.197	0.000	1.000	0.504
gambling_rt	assoc	lgbm	0.019	0.203	0.003	1.000	0.504
p_matrices	assoc	knn	0.021	0.237	0.001	1.000	0.504
emotion_rt	assoc	lgbm	0.004	0.193	0.001	1.000	0.504
language_perf	assoc	lgbm	0.089	0.197	0.007	1.000	0.504
gambling_rt	pred	lgbm	0.021	0.200	0.006	0.467	0.469
language_perf	embed_lgbm	elastic	0.073	0.201	0.003	0.088	0.455
language_perf	embed_lgbm	lgbm	0.056	0.201	0.002	0.088	0.455
int_g_like	embed_lgbm	elastic	0.104	0.192	0.010	0.080	0.414
language_perf	embed_linear	lgbm	0.090	0.197	0.007	0.410	0.386
emotion_rt	pred	lgbm	0.026	0.192	0.002	0.382	0.385
gambling_rt	embed_linear	lgbm	0.018	0.202	0.003	0.386	0.375
int_g_like	embed_linear	knn	0.073	0.195	0.007	0.443	0.369
int_g_like	embed_linear	elastic	0.067	0.192	0.010	0.443	0.369
int_g_like	embed_linear	lgbm	0.071	0.196	0.006	0.443	0.369
emotion_rt	embed_lgbm	elastic	0.026	0.193	0.001	0.022	0.367
emotion_rt	embed_linear	lgbm	0.032	0.191	0.003	0.357	0.357
emotion_rt	embed_linear	knn	0.012	0.194	0.000	0.357	0.357
int_g_like	pred	elastic	0.076	0.191	0.011	0.331	0.333
int_g_like	pred	lgbm	0.042	0.198	0.004	0.331	0.333
language_perf	pred	lgbm	0.087	0.197	0.007	0.324	0.325

Table 11: Proportion of CMC features selected for best performing models; p_sel_cmc = proportion of *all available* CMC features selected for final model; p_sel_feat_cmc = proportion of all *selected* features that are CMC features;

clearly exhibit interdependencies with one another. However, it should be noted that the relative maturation of each of these biomarkers may proceed at varying rates in any particular combination of brain region, subject or pathology. Gray matter (GM) volume is known to increase with age, as does the surface area, while cortical thickness thins with long-term development. These three biomarkers are inter-related, and existing studies focused on these measurements typically do not consider the inherent interdependence between their respective development, even though underlying interdependencies are inevitable. This paper presents a novel set of metrics that are based on cortical volume, surface area and thickness.

4.1 Interpretation of CMC and its potential relationship with macro-structural cortical development

The proposed (non-asymmetry) CMC features, defined in Equations 3 - 5, rely on underlying measurements of gray matter volume (measured in mm^3), surface area (measured in mm^2) and average cortical thickness (measured in mm). The nature of the proposed equations are such that they each produce an index, different values of which imply potentially major differences in the conformation of the local cortical region, potentially implying major differences in the tissue's historical neurodevelopment. When a cortical region exhibits a CMC measurement equal to 1, which is expected for sheet-like structures, that region exhibits a relatively simple cortical morphological presentation, and can be said to have high underlying cortical morphological congruence. Examples of this can be found consistently across subjects in brain structures such as the banks of the superior temporal sulcus ($\mu = 1.002, \sigma = 0.034$), and the insula ($\mu = 1.035, \sigma = 0.025$). When CMC values deviate from 1, this implies varying degrees of incongruence between the region's volumetric biomarkers and its surface area and cortical thickness biomarkers combined. The directionality of that incongruence (i.e. whether CMC is above or below 1) has major implications for the presentation of the conformation of that tissue, and implies differential cortical development has occurred.

When a cortical region exhibits CMC above 1, the GM volume has developed to be larger than the surface area times the mean thickness. This can occur when the overall growth of regional cortical tissue proceeds more quickly than increases in the surface area. Broadly speaking, the morphological structure that maximizes volume relative to surface area is the sphere. Thus, it is expected that convex (and thus partly spherical) presentation on the surface of the cortical region (well-rounded boundaries between the cortex and the pia mater which surrounds the cortex) will contribute to CMC measurements above 1. Regions such as the entorhinal cortex, which plays a role in working memory and thus is a highly relied upon region of cortical tissue, exhibits high CMC values ($\mu = 1.323, \sigma = 0.084$). This implies that the entorhinal region's development may have involved rapid increases in volume relative to its respective increases in surface area. These high CMC values may also implicate a distribution of pruning locations that supports sulcal formation, leading to more convex (partly spherical) local surface areas within the entorhinal cortex adjacent to locations of sulcal formation. Thus, we hypothesize that pruning in the entorhinal cortex has been more extensive (and possibly proceeded faster) than pruning in regions exhibiting cortical morphological congruence ($\text{CMC} = 1$) such as the banks of the superior temporal sulcus, or the insula. Results demonstrate that in addition to the entorhinal cortex, multiple regions exhibit consistently high mean CMC values, including the temporal pole ($\mu = 1.410$), frontal pole ($\mu = 1.384$), and pars orbitalis ($\mu = 1.281$).

When a cortical region exhibits CMC values below 1, the combination of the surface area times the mean thickness has developed to be larger than the gray matter volume. This can occur when the surface area, which is expected to be affected by several underlying factors, including regional brain growth, cortical folding and pruning, develops more rapidly than the growth in overall regional gray matter volume alone. Additionally, the distribution of locations of pruning within the cortex can result in the emergence of comparatively complex surfaces relative to the more spherical/convex surfaces already discussed, potentially resulting in comparatively large surface areas yielding reduced values for our CMC biomarkers. Regions such as the pericalcarine cortex exhibit low CMC values ($\mu = 0.965, \sigma = 0.025$), which could imply that surface area growth has outpaced corresponding volumetric growth in this region's development relative to other cortical regions.

4.2 Potential for CMC to characterize important aspects of brain development

The combination of regional cortical volume, surface area and mean thickness, biomarkers with relatively high variability across subjects, into a single CMC biomarker with relatively small variability in regional cortical measurements is noteworthy. Reliability and reproducibility are a major ongoing challenge in neuroscience research [Martínez et al., 2015, Marek et al., 2022], so any biomarkers that present consistently across a large population, and reliably demonstrate differential presentation across cortical regions, has considerable potential to assist in reliable and reproducible characterization of the human brain.

For most of the CMC biomarkers evaluated, males and females exhibit highly overlapping distributions, implying negligible differences in most cortical regions, which could imply the proposed biomarkers provide standardization benefits towards reproducible studies, and is consistent with largely overlapping functional abilities between the genders in most capacities. However, some male-female differences were observed in the temporal pole, the frontal pole and the pars opercularis, with females exhibiting higher CMC biomarkers on average than their male counterparts, though the distributions are still overlapping (see Figure 3 for an illustrative example).

The temporal pole has been implicated in many functions, including emotional processing [Córcoles-Parada et al., 2019], and the frontal pole has been reported to contribute to control over emotional approach-avoidance actions [Bramson et al., 2020]. Thus, gender differences in the presentation of the temporal and frontal poles, as assessed by CMC, may assist in characterization of known gender differences in emotional expression [Chaplin, 2015]. The pars opercularis is involved in language processing [Grewe et al., 2005], and sex differences in the pars opercularis, as assessed with CMC, may be indicative of underlying known differences in language development between males and females [Sato, 2020]. Indeed, it is encouraging that group-wise differences are observed in overlapping distributions as although we know sex effects exist in emotional expression and language development, there is a wide amount of variability in function across both genders, which is reflected in our CMC biomarker results exhibiting partially overlapping distributions between the sexes.

Although most cortical regions exhibited consistent CMC values in the left and right hemispheres, we did observe asymmetries in the transverse temporal, entorhinal, caudal anterior cingulate and pericalcarine regions. Asymmetries have previously been observed in the entorhinal cortex [Simic et al., 2005], with larger surface areas being reported in the left hemisphere. This is consistent with our findings of decreased CMC in the left hemisphere (increased surface area results in decreased CMC). The transverse temporal cortex is known to exhibit leftward asymmetries that are detectable by 31 weeks gestation [Chi et al., 1977], which is consistent with our findings of decreased CMC in the left hemisphere. Asymmetries have also been previously reported in the anterior cingulate [Yan et al., 2009]. The pericalcarine cortex has also been reported to exhibit asymmetries [Chiarello et al., 2016, Koelkebeck et al., 2014], which our analysis was also able to detect with CMC biomarkers. Our identification of asymmetries of CMC biomarkers implies that our analyses have considerable consistency with known asymmetric properties of the human brain.

4.3 Potential for CMC to characterize pathologies

A wide variety of pathological conditions have been demonstrated to exhibit abnormal phenotypic presentation of regions of the brain, including Down Syndrome [Levman et al., 2019b], attention deficit hyperactivity disorder (ADHD) [Huston et al., 2011, Stanley et al., 2008], schizophrenia [Innocenti et al., 2003, Keshavan et al., 1994, Feinberg, 1990, Hoffman and Dobscha, 1989, Rimol et al., 2010, Narr et al., 2005, Venkatasubramanian et al., 2008, Van Haren, 2011, Schultz et al., 2010, Nesvåg et al., 2008, Seitz et al., 2018, Qiu et al., 2010, Johnson et al., 2013, MacKinley et al., 2020], psychotic disorders [Bakker et al., 2016], autism [Khundrakpam et al., 2017, Pereira et al., 2018, Zielinski et al., 2014, Levman et al., 2019b, 2021], and multiple sclerosis [Brex et al., 2002, Losseff et al., 1996, Chen et al., 2004, Sailer, 2003, Levman et al., 2021].

Thus, future work will entail the characterization of the development of the pathological brain with CMC. As an additional novel biomarker not previously available, CMC may characterize regional abnormal development of the cortex in a manner not previously characterized, and the feature measurements generated by the approach outlined in this manuscript may also be a useful addition to future machine learning / artificial intelligence technologies that perform predictions for diagnostics, prognostics and treatment planning. Future work will investigate the potential for a variety of pathologies to be associated with macro-structural developmental abnormalities, such as aberrant folding and sulcal formation, and thus CMC may assist in the characterization of the macro-level phenotypic presentation of the brain. It is hoped that the CMC technique presented in this manuscript will be helpful in characterizing and understanding the developmental processes and etiological factors associated with healthy brain development, as well as a variety of neurodevelopmental disorders. It is also hoped that congruence based biomarkers will assist in characterizing important aspects of healthy and abnormal brain reliably and reproducibly.

5 Appendix A

hemi feature	left	right
frontalpole	43.3	76.4
entorhinal	115.6	65.8
temporalpole	129.4	114.6
transversetemporal	177.8	89.8
caudalanteriorcingulate	185.9	311.1
rostralanteriorcingulate	201.6	135.6
parsorbitalis	209.6	283.8
parahippocampal	244.1	206.1
bankssts	365.8	271.6
parstriangularis	485.1	402.0
paracentral	515.7	470.4
pericalcarine	533.5	458.9
posteriorcingulate	556.8	451.8
parsopercularis	594.0	360.8
cuneus	605.1	321.5
isthmuscingulate	672.6	457.8
medialorbitofrontal	688.7	507.9
insula	743.7	625.9
caudalmiddlefrontal	767.8	498.1
lateralorbitofrontal	902.2	718.0
middletemporal	966.3	873.2
inferiortemporal	1073.4	768.8
supramarginal	1236.4	960.8
superiortemporal	1258.2	1054.7
fusiform	1260.8	864.5
lingual	1383.5	1103.9
precuneus	1464.4	1196.5
inferiorparietal	1597.5	1611.7
postcentral	1836.3	1487.3
precentral	1997.2	1536.6
lateraloccipital	2085.5	1523.3
rostralmiddlefrontal	2136.7	2038.3
superiorparietal	2220.3	1947.2
superiorfrontal	2485.1	2077.1

Table 12: Ratios of ROI surface area divided by ROI average thickness.

6 Appendix B - Factor Targets

In the tables below, names follow HCP data naming conventions, unless otherwise indicated. The right column label indicates the name given to the single-factor synthetic target, and the right column values are the factor loadings. Factor loadings are the Pearson correlation between the original, unreduced variable (e.g. "gambling_task_perc_larger", below) and the final linear factor reduction (e.g. "gambling_perf", directly below).

_perf = test performance, i.e. test score _rt = reaction time, i.e. reaction times on a test wm = working memory

	gambling_perf
gambling_task_perc_larger	-1.0000
gambling_task_reward_perc_larger	-0.8926
gambling_task_punish_perc_larger	-0.8337

Table 13: Synthetic target `gambling-perf` factor loadings.

	emotion_perf
emotion_task_acc	-1.0000
emotion_task_shape_acc	-0.8952
emotion_task_face_acc	-0.8298

Table 14: Synthetic target `emotion-perf` factor loadings.

	language_rt
language_task_median_rt	1.0000
language_task_story_median_rt	0.8261
language_task_math_median_rt	0.8138

Table 15: Synthetic target `language-rt` factor loadings.

	relational_rt
relational_task_median_rt	-1.0000
relational_task_rel_median_rt	-0.9503
relational_task_match_median_rt	-0.8610

Table 16: Synthetic target `relational-rt` factor loadings.

	emotion_rt
emotion_task_median_rt	1.0000
emotion_task_face_median_rt	0.9528
emotion_task_shape_median_rt	0.9373

Table 17: Synthetic target `emotion-rt` factor loadings.

	language_perf
language_task_math_acc	-0.9975
language_task_acc	-0.8386
language_task_story_avg_difficulty_level	-0.7606

Table 18: Synthetic target `language-perf` factor loadings.

	p_matrices
p_matrices	1.0000
pmat24_a_cr	0.7158
pmat24_a_si	-0.7005

Table 19: Synthetic target `p-matrices` factor loadings.

	social_rt
social_task_median_rt_random	0.9838
social_task_random_median_rt_random	0.9826
social_task_tom_median_rt_tom	0.4105
social_task_median_rt_tom	0.4017

Table 20: Synthetic target `social-rt` factor loadings.

	psqi_latent
psqi_score	1.0000
psqi_comp1	0.6853
psqi_comp4	0.6379
psqi_comp3	0.6266
psqi_comp7	0.4649

Table 21: Synthetic target `psqi-latent` factor loadings.

	gambling_rt
gambling_task_median_rt_smaller	1.0000
gambling_task_reward_median_rt_smaller	0.9512
gambling_task_punish_median_rt_smaller	0.9504
gambling_task_median_rt_larger	0.8836
gambling_task_reward_median_rt_larger	0.8451
gambling_task_punish_median_rt_larger	0.8357

Table 22: Synthetic target `gambling-rt` factor loadings.

	social_random_perf
social_task_random_perc_random	-1.0000
social_task_perc_random	-0.9096
social_task_random_perc_unsure	0.8121
social_task_perc_unsure	0.7238
social_task_random_perc_tom	0.5595
social_task_perc_tom	0.3081
social_task_tom_perc_tom	-0.1047
social_task_tom_perc_unsure	0.0870
social_task_tom_perc_random	0.0638

Table 23: Synthetic target `social-random-perf` factor loadings.

	int_g_like
cogtotalcomp_unadj	-1.0000
cogearlycomp_unadj	-0.8750
cogfluidcomp_unadj	-0.8501
cogcrystalcomp_unadj	-0.7735
readeng_unadj	-0.7230
picvocab_unadj	-0.6767
listsort_unadj	-0.5698
cardsort_unadj	-0.5668
procspeed_unadj	-0.5640
flanker_unadj	-0.5116
picseq_unadj	-0.4938

Table 24: Synthetic target `int-g-like` factor loadings.

	neg_emotionality
percstress_unadj	0.8250
sadness_unadj	0.8165
loneliness_unadj	0.7812
neofac_n	0.7596
angaffect_unadj	0.7127
fearaffect_unadj	0.7000
percreject_unadj	0.6994
lifesatisf_unadj	-0.6571
posaffect_unadj	-0.6541
anghostil_unadj	0.6524
emotsupp_unadj	-0.6347
meanpurp_unadj	-0.6078
friendship_unadj	-0.5947
selfeff_unadj	-0.5589
perchostil_unadj	0.5512
neofac_e	-0.4649
instrusupp_unadj	-0.4578
neofac_a	-0.3779
fearsomat_unadj	0.3752

Table 25: Synthetic target `neg-emotionality` factor loadings.

	wm_rt
wm_task_median_rt	1.0000
wm_task_0bk_median_rt	0.9059
wm_task_2bk_median_rt	0.8999
wm_task_0bk_face_median_rt	0.7928
wm_task_0bk_tool_median_rt	0.7924
wm_task_0bk_body_median_rt	0.7914
wm_task_0bk_place_median_rt	0.7913
wm_task_0bk_tool_median_rt_nontarget	0.7911
wm_task_2bk_face_median_rt	0.7886
wm_task_0bk_face_median_rt_nontarget	0.7847
wm_task_0bk_place_median_rt_nontarget	0.7826
wm_task_0bk_body_median_rt_nontarget	0.7816
wm_task_2bk_place_median_rt	0.7638
wm_task_2bk_face_median_rt_nontarget	0.7573
wm_task_2bk_tool_median_rt	0.7409
wm_task_2bk_place_median_rt_nontarget	0.7372
wm_task_2bk_tool_median_rt_nontarget	0.7083
wm_task_2bk_body_median_rt	0.6629
wm_task_2bk_tool_median_rt_target	0.6306
wm_task_2bk_body_median_rt_nontarget	0.6159
wm_task_0bk_face_median_rt_target	0.5825
wm_task_2bk_face_median_rt_target	0.5699
wm_task_0bk_place_median_rt_target	0.5302

Table 26: Synthetic target `wm-rt` factor loadings.

	wm_perf
wm_task_acc	-0.9931
wm_task_0bk_acc	-0.8816
wm_task_2bk_acc	-0.7975
wm_task_0bk_body_acc	-0.7361
wm_task_0bk_tool_acc	-0.7269
wm_task_0bk_place_acc	-0.6881
wm_task_0bk_tool_acc_nontarget	-0.6827
wm_task_0bk_body_acc_nontarget	-0.6796
wm_task_0bk_face_acc	-0.6730
wm_task_2bk_body_acc	-0.6715
wm_task_0bk_face_acc_nontarget	-0.6543
wm_task_0bk_place_acc_nontarget	-0.6469
wm_task_2bk_face_acc	-0.6418
wm_task_2bk_tool_acc	-0.6395
wm_task_2bk_place_acc	-0.6326
wm_task_0bk_body_acc_target	-0.6263
wm_task_0bk_tool_acc_target	-0.5900
wm_task_2bk_body_acc_nontarget	-0.5782
wm_task_0bk_face_acc_target	-0.5502
wm_task_0bk_place_acc_target	-0.5501
wm_task_2bk_body_acc_target	-0.5481
wm_task_2bk_tool_acc_nontarget	-0.5383
wm_task_2bk_tool_acc_target	-0.4792
wm_task_2bk_face_acc_target	-0.4539
wm_task_2bk_place_acc_target	-0.4516

7 Appendix C

Table 27: Performance of models exceeding dummy model performance. FS = FreeSurfer features; CMC = CMC features; FS+CMC = both FS and CMC features used; wrap = forward stepwise feature selection with a linear model; assoc = feature selection by univariate association (mutual information); pred = feature selection by (linear) univariate prediction performance (accuracy); none = no feature selection (all features used in model) lgbm = LightGBM regressor; elastic = ElasticNet; r2 = coefficient of determination; mae = mean absolute error; mae+ = improvement in MAE relative to dummy model MAE;

target	feats	selection	model	r2	mae	mae+
int_g_like	FS	none	elastic	0.144	0.184	0.018
int_g_like	FS	assoc	elastic	0.143	0.184	0.018
int_g_like	FS	pred	elastic	0.143	0.184	0.018
int_g_like	FS	embed_linear	elastic	0.141	0.184	0.018
int_g_like	FS	embed_lgbm	elastic	0.141	0.189	0.013
int_g_like	FS	embed_linear	lgbm	0.132	0.191	0.011
int_g_like	FS	pred	lgbm	0.127	0.191	0.011
int_g_like	FS	none	lgbm	0.116	0.191	0.011
int_g_like	FS+CMC	assoc	lgbm	0.110	0.193	0.009
language_perf	FS	embed_linear	lgbm	0.106	0.194	0.010
int_g_like	CMC	embed_lgbm	elastic	0.104	0.191	0.011
int_g_like	FS+CMC	embed_lgbm	elastic	0.104	0.192	0.010
language_perf	FS	embed_lgbm	elastic	0.101	0.198	0.006
int_g_like	FS	embed_lgbm	lgbm	0.100	0.193	0.009
language_perf	CMC	embed_linear	lgbm	0.098	0.197	0.007
wm_perf	FS	embed_lgbm	lgbm	0.097	0.196	0.003
language_perf	FS	none	lgbm	0.095	0.195	0.008

Continued on next page

Table 27: Performance of models exceeding dummy model performance. FS = FreeSurfer features; CMC = CMC features; FS+CMC = both FS and CMC features used; wrap = forward stepwise feature selection with a linear model; assoc = feature selection by univariate association (mutual information); pred = feature selection by (linear) univariate prediction performance (accuracy); none = no feature selection (all features used in model) lgbm = LightGBM regressor; elastic = ElasticNet; r2 = coefficient of determination; mae = mean absolute error; mae+ = improvement in MAE relative to dummy model MAE;

target	feats	selection	model	r2	mae	mae+
wm_perf	FS	embed_lgbm	elastic	0.094	0.197	0.002
language_perf	CMC	assoc	lgbm	0.093	0.196	0.007
wm_perf	CMC	embed_linear	lgbm	0.093	0.197	0.002
wm_perf	FS	pred	lgbm	0.090	0.198	0.000
language_perf	FS+CMC	embed_linear	lgbm	0.090	0.197	0.007
language_perf	FS+CMC	assoc	lgbm	0.089	0.197	0.007
language_perf	FS+CMC	pred	lgbm	0.087	0.197	0.007
int_g_like	CMC	pred	lgbm	0.086	0.195	0.007
language_perf	CMC	pred	lgbm	0.086	0.197	0.007
language_perf	CMC	none	lgbm	0.085	0.197	0.006
language_perf	CMC	none	knn	0.084	0.198	0.006
int_g_like	FS+CMC	none	lgbm	0.084	0.195	0.007
int_g_like	CMC	assoc	lgbm	0.083	0.195	0.007
int_g_like	CMC	none	lgbm	0.083	0.196	0.006
language_perf	FS	pred	lgbm	0.080	0.198	0.005
int_g_like	CMC	embed_linear	lgbm	0.080	0.196	0.006
wm_perf	CMC	embed_lgbm	elastic	0.079	0.197	0.002
int_g_like	CMC	embed_linear	elastic	0.077	0.194	0.008
int_g_like	CMC	pred	elastic	0.076	0.194	0.008
int_g_like	FS+CMC	pred	elastic	0.076	0.191	0.011
int_g_like	FS+CMC	embed_linear	knn	0.073	0.195	0.007
int_g_like	FS	assoc	lgbm	0.073	0.196	0.006
int_g_like	CMC	none	elastic	0.073	0.194	0.008
int_g_like	CMC	assoc	elastic	0.073	0.194	0.008
language_perf	FS+CMC	embed_lgbm	elastic	0.073	0.201	0.003
int_g_like	FS+CMC	assoc	elastic	0.072	0.192	0.010
int_g_like	FS+CMC	none	elastic	0.071	0.192	0.010
int_g_like	FS+CMC	embed_linear	lgbm	0.071	0.196	0.006
language_perf	FS	assoc	lgbm	0.070	0.198	0.006
language_perf	FS	wrap	elastic	0.070	0.201	0.003
language_perf	FS+CMC	wrap	elastic	0.070	0.201	0.003
language_perf	FS+CMC	none	lgbm	0.068	0.200	0.003
int_g_like	FS+CMC	embed_linear	elastic	0.067	0.192	0.010
language_perf	FS	pred	elastic	0.065	0.203	0.001
language_perf	CMC	embed_lgbm	elastic	0.057	0.202	0.002
language_perf	FS+CMC	embed_lgbm	lgbm	0.056	0.201	0.002
language_perf	CMC	embed_lgbm	lgbm	0.050	0.202	0.001
int_g_like	CMC	wrap	elastic	0.050	0.198	0.004
int_g_like	FS+CMC	wrap	elastic	0.050	0.198	0.004
int_g_like	FS	wrap	elastic	0.050	0.198	0.004
language_perf	FS	embed_lgbm	lgbm	0.049	0.200	0.003
language_perf	CMC	wrap	elastic	0.048	0.202	0.002
emotion_rt	FS	embed_lgbm	lgbm	0.048	0.193	0.001
language_perf	CMC	wrap	lgbm	0.047	0.202	0.001
emotion_rt	FS	none	lgbm	0.046	0.190	0.004
int_g_like	FS	wrap	lgbm	0.044	0.198	0.004
emotion_rt	FS+CMC	none	lgbm	0.044	0.190	0.003
int_g_like	FS+CMC	wrap	lgbm	0.043	0.199	0.003
int_g_like	CMC	wrap	lgbm	0.042	0.199	0.003

Continued on next page

Table 27: Performance of models exceeding dummy model performance. FS = FreeSurfer features; CMC = CMC features; FS+CMC = both FS and CMC features used; wrap = forward stepwise feature selection with a linear model; assoc = feature selection by univariate association (mutual information); pred = feature selection by (linear) univariate prediction performance (accuracy); none = no feature selection (all features used in model) lgbm = LightGBM regressor; elastic = ElasticNet; r2 = coefficient of determination; mae = mean absolute error; mae+ = improvement in MAE relative to dummy model MAE;

target	feats	selection	model	r2	mae	mae+
int_g_like	FS+CMC	pred	lgbm	0.042	0.198	0.004
emotion_rt	FS	embed_linear	lgbm	0.041	0.190	0.004
emotion_rt	FS	assoc	lgbm	0.037	0.191	0.003
int_g_like	CMC	embed_lgbm	lgbm	0.036	0.197	0.005
p_matrices	FS+CMC	wrap	lgbm	0.036	0.237	0.002
p_matrices	FS+CMC	wrap	elastic	0.035	0.235	0.003
p_matrices	FS	wrap	elastic	0.035	0.235	0.003
p_matrices	CMC	wrap	elastic	0.033	0.234	0.004
emotion_rt	FS	wrap	elastic	0.032	0.191	0.003
emotion_rt	CMC	wrap	elastic	0.032	0.191	0.003
emotion_rt	FS+CMC	wrap	elastic	0.032	0.191	0.003
emotion_rt	FS+CMC	embed_linear	lgbm	0.032	0.191	0.003
int_g_like	FS+CMC	wrap	knn	0.031	0.200	0.002
emotion_rt	FS	pred	lgbm	0.030	0.192	0.002
p_matrices	FS	pred	lgbm	0.030	0.235	0.003
emotion_rt	CMC	embed_linear	lgbm	0.027	0.191	0.003
p_matrices	FS	wrap	lgbm	0.027	0.237	0.001
emotion_rt	FS+CMC	embed_lgbm	elastic	0.026	0.193	0.001
emotion_rt	FS+CMC	pred	lgbm	0.026	0.192	0.002
wm_rt	CMC	pred	lgbm	0.025	0.195	0.002
emotion_rt	CMC	assoc	lgbm	0.025	0.192	0.002
p_matrices	FS	embed_linear	lgbm	0.024	0.237	0.002
p_matrices	FS	none	lgbm	0.024	0.237	0.001
emotion_rt	CMC	pred	lgbm	0.023	0.192	0.002
p_matrices	FS	assoc	lgbm	0.023	0.237	0.001
p_matrices	FS+CMC	assoc	knn	0.021	0.237	0.001
gambling_rt	FS+CMC	pred	lgbm	0.021	0.200	0.006
wm_rt	FS	none	lgbm	0.021	0.195	0.002
gambling_rt	FS+CMC	assoc	lgbm	0.019	0.203	0.003
gambling_rt	FS+CMC	embed_linear	lgbm	0.018	0.202	0.003
int_g_like	CMC	wrap	knn	0.018	0.199	0.003
wm_rt	FS+CMC	assoc	lgbm	0.016	0.197	0.000
gambling_rt	FS+CMC	wrap	elastic	0.015	0.203	0.003
gambling_rt	CMC	wrap	elastic	0.015	0.203	0.003
p_matrices	FS+CMC	none	lgbm	0.015	0.238	0.001
p_matrices	FS+CMC	assoc	lgbm	0.015	0.237	0.002
gambling_rt	FS	embed_linear	lgbm	0.014	0.203	0.003
wm_rt	CMC	none	lgbm	0.014	0.197	0.000
p_matrices	CMC	embed_lgbm	knn	0.013	0.236	0.002
gambling_rt	CMC	pred	lgbm	0.013	0.203	0.002
p_matrices	FS	embed_lgbm	elastic	0.013	0.238	0.000
gambling_rt	FS+CMC	wrap	lgbm	0.013	0.204	0.002
emotion_rt	FS+CMC	embed_linear	knn	0.012	0.194	0.000
gambling_rt	FS	wrap	elastic	0.011	0.204	0.002
gambling_rt	FS	wrap	lgbm	0.011	0.204	0.002
emotion_rt	CMC	wrap	lgbm	0.010	0.194	0.000
emotion_rt	FS	wrap	lgbm	0.009	0.193	0.001
gambling_rt	CMC	none	lgbm	0.009	0.204	0.002
gambling_rt	FS	none	lgbm	0.008	0.205	0.000

Continued on next page

Table 27: Performance of models exceeding dummy model performance. FS = FreeSurfer features; CMC = CMC features; FS+CMC = both FS and CMC features used; wrap = forward stepwise feature selection with a linear model; assoc = feature selection by univariate association (mutual information); pred = feature selection by (linear) univariate prediction performance (accuracy); none = no feature selection (all features used in model) lgbm = LightGBM regressor; elastic = ElasticNet; r2 = coefficient of determination; mae = mean absolute error; mae+ = improvement in MAE relative to dummy model MAE;

target	feats	selection	model	r2	mae	mae+
gambling_rt	CMC	embed_linear	lgbm	0.008	0.204	0.002
emotion_rt	FS+CMC	wrap	lgbm	0.007	0.194	0.000
gambling_rt	CMC	assoc	lgbm	0.006	0.205	0.001
gambling_perf	FS	none	lgbm	0.006	0.166	0.000
wm_rt	CMC	wrap	elastic	0.006	0.196	0.001
wm_rt	FS+CMC	wrap	elastic	0.006	0.196	0.001
gambling_rt	CMC	embed_lgbm	elastic	0.005	0.205	0.001
emotion_rt	FS+CMC	assoc	lgbm	0.004	0.193	0.001
p_matrices	CMC	assoc	lgbm	0.004	0.237	0.001
gambling_perf	CMC	wrap	elastic	0.003	0.165	0.001
language_rt	FS	wrap	lgbm	0.002	0.190	0.000
social_rt	FS	embed_lgbm	lgbm	0.001	0.194	0.000
social_rt	FS	wrap	elastic	0.001	0.194	0.000
gambling_perf	FS	embed_linear	lgbm	0.001	0.166	0.000

References

Jessica Dubois, Marianne Alison, Serena J. Counsell, Lucie Hertz-Pannier, Petra S. Hüppi, and Manon J.N.L. Benders. MRI of the Neonatal Brain: A Review of Methodological Challenges and Neuroscientific Advances. *Journal of Magnetic Resonance Imaging*, 53(5):1318–1343, May 2021. ISSN 1053-1807, 1522-2586. doi:10.1002/jmri.27192. URL `https://onlinelibrary.wiley.com/doi/10.1002/jmri.27192`.

Bruce Fischl. FreeSurfer. *NeuroImage*, 62(2):774–781, August 2012. ISSN 10538119. doi:10.1016/j.neuroimage.2012.01.021. URL `https://linkinghub.elsevier.com/retrieve/pii/S1053811912000389`.

Jacob Levman, Patrick MacDonald, Ashley Ruyan Lim, Cynthia Forgeron, and Emi Takahashi. A pediatric structural MRI analysis of healthy brain development from newborns to young adults. *Human Brain Mapping*, 38(12):5931–5942, December 2017. ISSN 1065-9471, 1097-0193. doi:10.1002/hbm.23799. URL `https://onlinelibrary.wiley.com/doi/10.1002/hbm.23799`.

Jacob Levman, Patrick MacDonald, Sean Rowley, Natalie Stewart, Ashley Lim, Bryan Ewenson, Albert Galaburda, and Emi Takahashi. Structural Magnetic Resonance Imaging Demonstrates Abnormal Regionally-Differential Cortical Thickness Variability in Autism: From Newborns to Adults. *Frontiers in Human Neuroscience*, 13:75, March 2019a. ISSN 1662-5161. doi:10.3389/fnhum.2019.00075. URL `https://www.frontiersin.org/article/10.3389/fnhum.2019.00075/full`.

Bernadette McCann, Jacob Levman, Nicole Baumer, Melanie Y. Lam, Tadashi Shiohama, Liam Cogger, Allissa MacDonald, Prahar Ijner, and Emi Takahashi. Structural magnetic resonance imaging demonstrates volumetric brain abnormalities in down syndrome: Newborns to young adults. *NeuroImage: Clinical*, 32:102815, 2021. ISSN 22131582. doi:10.1016/j.nicl.2021.102815. URL `https://linkinghub.elsevier.com/retrieve/pii/S221315822100259X`.

Kenia Martínez, Sarah K. Madsen, Anand A. Joshi, Shantanu H. Joshi, Francisco J. Román, Julio Villalon-Reina, Miguel Burgaleta, Sherif Karama, Joost Janssen, Eugenio Marinetto, Manuel Desco, Paul M. Thompson, and Roberto Colom. Reproducibility of brain-cognition relationships using three cortical surface-based protocols: An exhaustive analysis based on cortical thickness: Reproducibility of Brain-Cognition Relationships. *Human Brain Mapping*, 36 (8):3227–3245, August 2015. ISSN 10659471. doi:10.1002/hbm.22843. URL `https://onlinelibrary.wiley.com/doi/10.1002/hbm.22843`.

Scott Marek, Brenden Tervo-Clemmens, Finnegan J. Calabro, David F. Montez, Benjamin P. Kay, Alexander S. Hatoum, Meghan Rose Donohue, William Foran, Ryland L. Miller, Timothy J. Hendrickson, Stephen M. Malone, Sridhar Kandala, Eric Feczko, Oscar Miranda-Dominguez, Alice M. Graham, Eric A. Earl, Anders J. Perrone, Michaela Cordova, Olivia Doyle, Lucille A. Moore, Gregory M. Conan, Johnny Uriarte, Kathy Snider, Benjamin J. Lynch, James C. Wilgenbusch, Thomas Pengo, Angela Tam, Jianzhong Chen, Dillan J. Newbold, Annie Zheng, Nicole A. Seider, Andrew N. Van, Athanasia Metoki, Roselyne J. Chauvin, Timothy O. Laumann, Deanna J. Greene, Steven E. Petersen, Hugh Garavan, Wesley K. Thompson, Thomas E. Nichols, B. T. Thomas Yeo, Deanna M. Barch, Beatriz Luna, Damien A. Fair, and Nico U. F. Dosenbach. Reproducible brain-wide association studies require thousands of individuals. *Nature*, 603(7902):654–660, March 2022. ISSN 0028-0836, 1476-4687. doi:10.1038/s41586-022-04492-9. URL https://www.nature.com/articles/s41586-022-04492-9.

P. Buisseret. Chapter 22 The development of visual cortical properties depends on visuo-proprioceptive congruence. In *Progress in Brain Research*, volume 95, pages 251–256. Elsevier, 1993. ISBN 978-0-444-89492-2. doi:10.1016/S0079-6123(08)60373-8. URL https://linkinghub.elsevier.com/retrieve/pii/S0079612308603738.

Manula A. Somaratna and Alan W. Freeman. A model for the development of binocular congruence in primary visual cortex. *Scientific Reports*, 12(1):12669, July 2022. ISSN 2045-2322. doi:10.1038/s41598-022-16739-6. URL https://www.nature.com/articles/s41598-022-16739-6.

Jo Edwards-Duric, Richard J. Stevenson, and Heather M. Francis. The congruence of interoceptive predictions and hippocampal-related memory. *Biological Psychology*, 155:107929, September 2020. ISSN 03010511. doi:10.1016/j.biopsycho.2020.107929. URL https://linkinghub.elsevier.com/retrieve/pii/S0301051120300892.

Daniel Stubbs, Jamin DeProto, Kai Nie, Chris Englund, Imran Mahmud, Robert Hevner, and Zoltán Molnár. Neurovascular Congruence during Cerebral Cortical Development. *Cerebral Cortex*, 19(suppl_1):i32–i41, July 2009. ISSN 1460-2199, 1047-3211. doi:10.1093/cercor/bhp040. URL https://academic.oup.com/cercor/article-lookup/doi/10.1093/cercor/bhp040.

Kathleen Kang, Robert Rosenkranz, Kaan Karan, Ercan Altinsoy, and Shu-Chen Li. Congruence-based contextual plausibility modulates cortical activity during vibrotactile perception in virtual multisensory environments. *Communications Biology*, 5(1):1360, December 2022. ISSN 2399-3642. doi:10.1038/s42003-022-04318-4. URL https://www.nature.com/articles/s42003-022-04318-4.

Tao Yao and Wim Vanduffel. Neuronal congruency effects in macaque prefrontal cortex. *Nature Communications*, 13(1):4702, August 2022. ISSN 2041-1723. doi:10.1038/s41467-022-32382-1. URL https://www.nature.com/articles/s41467-022-32382-1.

Kiho Im, Jong-Min Lee, Oliver Lyttelton, Sun Hyung Kim, Alan C. Evans, and Sun I. Kim. Brain Size and Cortical Structure in the Adult Human Brain. *Cerebral Cortex*, 18(9):2181–2191, September 2008. ISSN 1047-3211. doi:10.1093/cercor/bhm244. URL https://doi.org/10.1093/cercor/bhm244.

Jennifer Stine Elam, Matthew F. Glasser, Michael P. Harms, Stamatios N. Sotiropoulos, Jesper L.R. Andersson, Gregory C. Burgess, Sandra W. Curtiss, Robert Oostenveld, Linda J. Larson-Prior, Jan-Mathijs Schoffelen, Michael R. Hodge, Eileen A. Cler, Daniel M. Marcus, Deanna M. Barch, Essa Yacoub, Stephen M. Smith, Kamil Ugurbil, and David C. Van Essen. The Human Connectome Project: A retrospective. *NeuroImage*, 244:118543, December 2021. ISSN 10538119. doi:10.1016/j.neuroimage.2021.118543. URL https://linkinghub.elsevier.com/retrieve/pii/S1053811921008168.

Rahul S. Desikan, Florent Ségonne, Bruce Fischl, Brian T. Quinn, Bradford C. Dickerson, Deborah Blacker, Randy L. Buckner, Anders M. Dale, R. Paul Maguire, Bradley T. Hyman, Marilyn S. Albert, and Ronald J. Killiany. An automated labeling system for subdividing the human cerebral cortex on MRI scans into gyral based regions of interest. *NeuroImage*, 31(3):968–980, July 2006. ISSN 1053-8119. doi:10.1016/j.neuroimage.2006.01.021.

Douglas G. Bonett. Confidence interval for a coefficient of quartile variation. *Computational Statistics & Data Analysis*, 50(11):2953–2957, July 2006. ISSN 0167-9473. doi:10.1016/j.csda.2005.05.007. URL https://www.sciencedirect.com/science/article/pii/S0167947305001271.

Ricardo J. G. B. Campello, Davoud Moulavi, Arthur Zimek, and Jörg Sander. Hierarchical Density Estimates for Data Clustering, Visualization, and Outlier Detection. *ACM Transactions on Knowledge Discovery from Data*, 10(1):5:1–5:51, July 2015. ISSN 1556-4681. doi:10.1145/2733381. URL https://doi.org/10.1145/2733381.

Fabian Pedregosa, Gaël Varoquaux, Alexandre Gramfort, Vincent Michel, Bertrand Thirion, Olivier Grisel, Mathieu Blondel, Peter Prettenhofer, Ron Weiss, Vincent Dubourg, Jake Vanderplas, Alexandre Passos, David Cournapeau, Matthieu Brucher, Matthieu Perrot, and Édouard Duchesnay. Scikit-learn: Machine learning in python. *Journal of Machine Learning Research*, 12(85):2825–2830, 2011. URL http://jmlr.org/papers/v12/pedregosa11a.html.

Raymond B. Cattell. *The Scientific Use of Factor Analysis in Behavioral and Life Sciences*. Springer US, Boston, MA, 1978. ISBN 978-1-4684-2264-1 978-1-4684-2262-7. doi:10.1007/978-1-4684-2262-7. URL http://link.springer.com/10.1007/978-1-4684-2262-7.

Dennis Child. *The Essentials of Factor Analysis*. Bloomsbury Academic, London ; New York, 3rd edition edition, June 2006. ISBN 978-0-8264-8000-2.

H. Attias. Independent Factor Analysis. *Neural Computation*, 11(4):803–851, May 1999. ISSN 0899-7667. doi:10.1162/089976699300016458. URL https://doi.org/10.1162/089976699300016458.

Deanna M. Barch, Gregory C. Burgess, Michael P. Harms, Steven E. Petersen, Bradley L. Schlaggar, Maurizio Corbetta, Matthew F. Glasser, Sandra Curtiss, Sachin Dixit, Cindy Feldt, Dan Nolan, Edward Bryant, Tucker Hartley, Owen Footer, James M. Bjork, Russ Poldrack, Steve Smith, Heidi Johansen-Berg, Abraham Z. Snyder, and David C. Van Essen. Function in the human connectome: Task-fMRI and individual differences in behavior. *NeuroImage*, 80:169–189, October 2013. ISSN 1053-8119. doi:10.1016/j.neuroimage.2013.05.033. URL http://dx.doi.org/10.1016/j.neuroimage.2013.05.033.

D. J. Buysse, C. F. Reynolds, T. H. Monk, S. R. Berman, and D. J. Kupfer. The Pittsburgh Sleep Quality Index: A new instrument for psychiatric practice and research. *Psychiatry Research*, 28(2):193–213, May 1989. ISSN 0165-1781. doi:10.1016/0165-1781(89)90047-4.

Guolin Ke, Qi Meng, Thomas Finley, Taifeng Wang, Wei Chen, Weidong Ma, Qiwei Ye, and Tie-Yan Liu. LightGBM: A highly efficient gradient boosting decision tree. In I. Guyon, U. Von Luxburg, S. Bengio, H. Wallach, R. Fergus, S. Vishwanathan, and R. Garnett, editors, *Advances in Neural Information Processing Systems*, volume 30. Curran Associates, Inc., 2017. URL https://proceedings.neurips.cc/paper_files/paper/2017/file/6449f44a102fde848669bdd9eb6b76fa-Paper.pdf.

Jason Ansel, Edward Yang, Horace He, Natalia Gimelshein, Animesh Jain, Michael Voznesensky, Bin Bao, Peter Bell, David Berard, Evgeni Burovski, Geeta Chauhan, Anjali Chourdia, Will Constable, Alban Desmaison, Zachary DeVito, Elias Ellison, Will Feng, Jiong Gong, Michael Gschwind, Brian Hirsh, Sherlock Huang, Kshiteej Kalambarkar, Laurent Kirsch, Michael Lazos, Mario Lezcano, Yanbo Liang, Jason Liang, Yinghai Lu, C. K. Luk, Bert Maher, Yunjie Pan, Christian Puhrsch, Matthias Reso, Mark Saroufim, Marcos Yukio Siraichi, Helen Suk, Shunting Zhang, Michael Suo, Phil Tillet, Xu Zhao, Eikan Wang, Keren Zhou, Richard Zou, Xiaodong Wang, Ajit Mathews, William Wen, Gregory Chanan, Peng Wu, and Soumith Chintala. PyTorch 2: Faster machine learning through dynamic python bytecode transformation and graph compilation. In *Proceedings of the 29th ACM International Conference on Architectural Support for Programming Languages and Operating Systems, Volume 2*, Asplos '24. ACM, April 2024. doi:10.1145/3620665.3640366. URL http://dx.doi.org/10.1145/3620665.3640366.

Jacob Levman, Maxwell Jennings, Ethan Rouse, Derek Berger, Priya Kabaria, Masahito Nangaku, Iker Gondra, and Emi Takahashi. A morphological study of schizophrenia with magnetic resonance imaging, advanced analytics, and machine learning. *Frontiers in Neuroscience*, 16:926426, August 2022. ISSN 1662-453X. doi:10.3389/fnins.2022.926426. URL https://www.frontiersin.org/articles/10.3389/fnins.2022.926426/full.

Hui Zou and Trevor Hastie. Regularization and variable selection via the elastic net. *Journal of the Royal Statistical Society Series B: Statistical Methodology*, 67(2):301–320, March 2005. ISSN 1467-9868. doi:10.1111/j.1467-9868.2005.00503.x. URL http://dx.doi.org/10.1111/j.1467-9868.2005.00503.x.

Takuya Akiba, Shotaro Sano, Toshihiko Yanase, Takeru Ohta, and Masanori Koyama. Optuna: A next-generation hyperparameter optimization framework, 2019. URL https://arxiv.org/abs/1907.10902.

DM-Berger. Stfxecutables/cortical_congruence: Init. Zenodo, July 2024. URL https://zenodo.org/doi/10.5281/zenodo.13146453.

Marta Córcoles-Parada, Mar Ubero-Martínez, Richard G. M. Morris, Ricardo Insausti, Mortimer Mishkin, and Mónica Muñoz-López. Frontal and Insular Input to the Dorsolateral Temporal Pole in Primates: Implications for Auditory Memory. *Frontiers in Neuroscience*, 13:1099, November 2019. ISSN 1662-453X. doi:10.3389/fnins.2019.01099. URL https://www.frontiersin.org/article/10.3389/fnins.2019.01099/full.

Bob Bramson, Davide Folloni, Lennart Verhagen, Bart Hartogsveld, Rogier B. Mars, Ivan Toni, and Karin Roelofs. Human Lateral Frontal Pole Contributes to Control over Emotional Approach–Avoidance Actions. *The Journal of Neuroscience*, 40(14):2925–2934, April 2020. ISSN 0270-6474, 1529-2401. doi:10.1523/JNEUROSCI.2048-19.2020. URL https://www.jneurosci.org/lookup/doi/10.1523/JNEUROSCI.2048-19.2020.

Tara M. Chaplin. Gender and Emotion Expression: A Developmental Contextual Perspective. *Emotion Review*, 7(1): 14–21, January 2015. ISSN 1754-0739, 1754-0747. doi:10.1177/1754073914544408. URL http://journals.sagepub.com/doi/10.1177/1754073914544408.

Tanja Grewe, Ina Bornkessel, Stefan Zysset, Richard Wiese, D. Yves Von Cramon, and Matthias Schlesewsky. The emergence of the unmarked: A new perspective on the language-specific function of Broca's area. *Human Brain Mapping*, 26(3):178–190, November 2005. ISSN 1065-9471, 1097-0193. doi:10.1002/hbm.20154. URL https://onlinelibrary.wiley.com/doi/10.1002/hbm.20154.

Marc Sato. The neurobiology of sex differences during language processing in healthy adults: A systematic review and a meta-analysis. *Neuropsychologia*, 140:107404, March 2020. ISSN 00283932. doi:10.1016/j.neuropsychologia.2020.107404. URL https://linkinghub.elsevier.com/retrieve/pii/S0028393220300750.

G. Simic, S. Bexheti, Z. Kelovic, M. Kos, K. Grbic, P.R. Hof, and I. Kostovic. Hemispheric asymmetry, modular variability and age-related changes in the human entorhinal cortex. *Neuroscience*, 130(4):911–925, January 2005. ISSN 03064522. doi:10.1016/j.neuroscience.2004.09.040. URL https://linkinghub.elsevier.com/retrieve/pii/S0306452204008772.

J. G. Chi, E. C. Dooling, and F. H. Gilles. Left-Right Asymmetries of the Temporal Speech Areas of the Human Fetus. *Archives of Neurology*, 34(6):346–348, June 1977. ISSN 0003-9942. doi:10.1001/archneur.1977.00500180040008. URL http://archneur.jamanetwork.com/article.aspx?articleid=575612.

Hao Yan, Xi-Nian Zuo, Deyi Wang, Jue Wang, Chaozhe Zhu, Michael P. Milham, Dai Zhang, and Yufeng Zang. Hemispheric asymmetry in cognitive division of anterior cingulate cortex: A resting-state functional connectivity study. *NeuroImage*, 47(4):1579–1589, October 2009. ISSN 10538119. doi:10.1016/j.neuroimage.2009.05.080. URL https://linkinghub.elsevier.com/retrieve/pii/S1053811909005965.

Christine Chiarello, David Vazquez, Adam Felton, and Alessandra McDowell. Structural asymmetry of the human cerebral cortex: Regional and between-subject variability of surface area, cortical thickness, and local gyrification. *Neuropsychologia*, 93:365–379, December 2016. ISSN 00283932. doi:10.1016/j.neuropsychologia.2016.01.012. URL https://linkinghub.elsevier.com/retrieve/pii/S0028393216300124.

Katja Koelkebeck, Jun Miyata, Manabu Kubota, Waldemar Kohl, Shuraku Son, Hidenao Fukuyama, Nobukatsu Sawamoto, Hidehiko Takahashi, and Toshiya Murai. The contribution of cortical thickness and surface area to gray matter asymmetries in the healthy human brain: Gray Matter Asymmetries in the Human Brain. *Human Brain Mapping*, 35(12):6011–6022, December 2014. ISSN 10659471. doi:10.1002/hbm.22601. URL https://onlinelibrary.wiley.com/doi/10.1002/hbm.22601.

Jacob Levman, Allissa MacDonald, Nicole Baumer, Patrick MacDonald, Natalie Stewart, Ashley Lim, Liam Cogger, Tadashi Shiohama, and Emi Takahashi. Structural magnetic resonance imaging demonstrates abnormal cortical thickness in Down syndrome: Newborns to young adults. *NeuroImage: Clinical*, 23:101874, 2019b. ISSN 22131582. doi:10.1016/j.nicl.2019.101874. URL https://linkinghub.elsevier.com/retrieve/pii/S2213158219302244.

Conor Liston, Matthew Malter Cohen, Theresa Teslovich, Daniel Levenson, and B.J. Casey. Atypical Prefrontal Connectivity in Attention-Deficit/Hyperactivity Disorder: Pathway to Disease or Pathological End Point? *Biological Psychiatry*, 69(12):1168–1177, June 2011. ISSN 00063223. doi:10.1016/j.biopsych.2011.03.022. URL https://linkinghub.elsevier.com/retrieve/pii/S0006322311002708.

Jeffrey A. Stanley, Heidi Kipp, Erika Greisenegger, Frank P. MacMaster, K. Panchalingam, Matcheri S. Keshavan, Oscar G. Bukstein, and Jay W. Pettegrew. Evidence of Developmental Alterations in Cortical and Subcortical Regions of Children With Attention-Deficit/Hyperactivity Disorder: A Multivoxel In Vivo Phosphorus 31 Spectroscopy Study. *Archives of General Psychiatry*, 65(12):1419, December 2008. ISSN 0003-990X. doi:10.1001/archgenpsychiatry.2008.503. URL http://archpsyc.jamanetwork.com/article.aspx?doi=10.1001/archgenpsychiatry.2008.503.

G M Innocenti, F Ansermet, and J Parnas. Schizophrenia, neurodevelopment and corpus callosum. *Molecular Psychiatry*, 8(3):261–274, March 2003. ISSN 1359-4184, 1476-5578. doi:10.1038/sj.mp.4001205. URL https://www.nature.com/articles/4001205.

Matcheri S. Keshavan, Stewart Anderson, and Jay W. Pettergrew. Is Schizophrenia due to excessive synaptic pruning in the prefrontal cortex? The Feinberg hypothesis revisited. *Journal of Psychiatric Research*, 28(3):239–265, May 1994. ISSN 00223956. doi:10.1016/0022-3956(94)90009-4. URL https://linkinghub.elsevier.com/retrieve/pii/0022395694900094.

I. Feinberg. Cortical Pruning and the Development of Schizophrenia. *Schizophrenia Bulletin*, 16(4):567–568, January 1990. ISSN 0586-7614, 1745-1701. doi:10.1093/schbul/16.4.567. URL https://academic.oup.com/schizophreniabulletin/article-lookup/doi/10.1093/schbul/16.4.567.

R. E. Hoffman and S. K. Dobscha. Cortical Pruning and the Development of Schizophrenia: A Computer Model. *Schizophrenia Bulletin*, 15(3):477–490, January 1989. ISSN 0586-7614, 1745-1701. doi:10.1093/schbul/15.3.477. URL https://academic.oup.com/schizophreniabulletin/article-lookup/doi/10.1093/schbul/15.3.477.

Lars M. Rimol, Cecilie B. Hartberg, Ragnar Nesvåg, Christine Fennema-Notestine, Donald J. Hagler, Chris J. Pung, Robin G. Jennings, Unn K. Haukvik, Elisabeth Lange, Per H. Nakstad, Ingrid Melle, Ole A. Andreassen, Anders M.

Dale, and Ingrid Agartz. Cortical Thickness and Subcortical Volumes in Schizophrenia and Bipolar Disorder. *Biological Psychiatry*, 68(1):41–50, July 2010. ISSN 00063223. doi:10.1016/j.biopsych.2010.03.036. URL https://linkinghub.elsevier.com/retrieve/pii/S0006322310003501.

Katherine L. Narr, Robert M. Bilder, Arthur W. Toga, Roger P. Woods, David E. Rex, Philip R. Szeszko, Delbert Robinson, Serge Sevy, Handan Gunduz-Bruce, Yung-Ping Wang, Heather DeLuca, and Paul M. Thompson. Mapping Cortical Thickness and Gray Matter Concentration in First Episode Schizophrenia. *Cerebral Cortex*, 15(6):708–719, June 2005. ISSN 1460-2199, 1047-3211. doi:10.1093/cercor/bhh172. URL http://academic.oup.com/cercor/article/15/6/708/495578/Mapping-Cortical-Thickness-and-Gray-Matter.

G. Venkatasubramanian, P. N. Jayakumar, B. N. Gangadhar, and M. S. Keshavan. Automated MRI parcellation study of regional volume and thickness of prefrontal cortex (PFC) in antipsychotic-naïve schizophrenia. *Acta Psychiatrica Scandinavica*, 117(6):420–431, June 2008. ISSN 0001-690X, 1600-0447. doi:10.1111/j.1600-0447.2008.01198.x. URL https://onlinelibrary.wiley.com/doi/10.1111/j.1600-0447.2008.01198.x.

Neeltje E. M. Van Haren. Changes in Cortical Thickness During the Course of Illness in Schizophrenia. *Archives of General Psychiatry*, 68(9):871, September 2011. ISSN 0003-990X. doi:10.1001/archgenpsychiatry.2011.88. URL http://archpsyc.jamanetwork.com/article.aspx?doi=10.1001/archgenpsychiatry.2011.88.

C. Christoph Schultz, Kathrin Koch, Gerd Wagner, Martin Roebel, Claudia Schachtzabel, Christian Gaser, Igor Nenadic, Jürgen R. Reichenbach, Heinrich Sauer, and Ralf G.M. Schlösser. Reduced cortical thickness in first episode schizophrenia. *Schizophrenia Research*, 116(2-3):204–209, February 2010. ISSN 09209964. doi:10.1016/j.schres.2009.11.001. URL https://linkinghub.elsevier.com/retrieve/pii/S0920996409005489.

Ragnar Nesvåg, Glenn Lawyer, Katarina Varnäs, Anders M. Fjell, Kristine B. Walhovd, Arnoldo Frigessi, Erik G. Jönsson, and Ingrid Agartz. Regional thinning of the cerebral cortex in schizophrenia: Effects of diagnosis, age and antipsychotic medication. *Schizophrenia Research*, 98(1-3):16–28, January 2008. ISSN 09209964. doi:10.1016/j.schres.2007.09.015. URL https://linkinghub.elsevier.com/retrieve/pii/S0920996407004069.

Johanna Seitz, Yogesh Rathi, Amanda Lyall, Ofer Pasternak, Elisabetta C. Del Re, Margaret Niznikiewicz, Paul Nestor, Larry J. Seidman, Tracey L. Petryshen, Raquelle I. Mesholam-Gately, Joanne Wojcik, Robert W. McCarley, Martha E. Shenton, Inga K. Koerte, and Marek Kubicki. Alteration of gray matter microstructure in schizophrenia. *Brain Imaging and Behavior*, 12(1):54–63, February 2018. ISSN 1931-7557, 1931-7565. doi:10.1007/s11682-016-9666-7. URL http://link.springer.com/10.1007/s11682-016-9666-7.

Anqi Qiu, Ta Anh Tuan, Puay San Woon, Muhammad Farid Abdul-Rahman, Steven Graham, and Kang Sim. Hippocampal-cortical structural connectivity disruptions in schizophrenia: An integrated perspective from hippocampal shape, cortical thickness, and integrity of white matter bundles. *NeuroImage*, 52(4):1181–1189, October 2010. ISSN 10538119. doi:10.1016/j.neuroimage.2010.05.046. URL https://linkinghub.elsevier.com/retrieve/pii/S1053811910007780.

Sarah L.M. Johnson, Lei Wang, Kathryn I. Alpert, Deanna Greenstein, Liv Clasen, Francois Lalonde, Rachel Miller, Judith Rapoport, and Nitin Gogtay. Hippocampal Shape Abnormalities of Patients With Childhood-Onset Schizophrenia and Their Unaffected Siblings. *Journal of the American Academy of Child & Adolescent Psychiatry*, 52(5):527–536.e2, May 2013. ISSN 08908567. doi:10.1016/j.jaac.2013.02.003. URL https://linkinghub.elsevier.com/retrieve/pii/S089085671300107X.

Michael Lloyd MacKinley, Priyadharshini Sabesan, and Lena Palaniyappan. Deviant cortical sulcation related to schizophrenia and cognitive deficits in the second trimester. *Translational Neuroscience*, 11(1):236–240, July 2020. ISSN 2081-6936. doi:10.1515/tnsci-2020-0111. URL https://www.degruyter.com/document/doi/10.1515/tnsci-2020-0111/html.

Geor Bakker, Matthan W. A. Caan, Wilhelmina A. M. Vingerhoets, Fabiana Da Silva- Alves, Mariken De Koning, Erik Boot, Dorien H. Nieman, Lieuwe De Haan, Oswald J. Bloemen, Jan Booij, and Thérèse A. M. J. Van Amelsvoort. Cortical Morphology Differences in Subjects at Increased Vulnerability for Developing a Psychotic Disorder: A Comparison between Subjects with Ultra-High Risk and 22q11.2 Deletion Syndrome. *PLOS ONE*, 11(11):e0159928, November 2016. ISSN 1932-6203. doi:10.1371/journal.pone.0159928. URL https://dx.plos.org/10.1371/journal.pone.0159928.

Budhachandra S. Khundrakpam, John D. Lewis, Penelope Kostopoulos, Felix Carbonell, and Alan C. Evans. Cortical Thickness Abnormalities in Autism Spectrum Disorders Through Late Childhood, Adolescence, and Adulthood: A Large-Scale MRI Study. *Cerebral Cortex*, 27(3):1721–1731, March 2017. ISSN 1047-3211, 1460-2199. doi:10.1093/cercor/bhx038. URL https://academic.oup.com/cercor/article-lookup/doi/10.1093/cercor/bhx038.

Alessandra M. Pereira, Brunno M. Campos, Ana C. Coan, Luiz F. Pegoraro, Thiago J. R. De Rezende, Ignacio Obeso, Paulo Dalgalarrondo, Jaderson C. Da Costa, Jean-Claude Dreher, and Fernando Cendes. Differences in Cortical Structure and Functional MRI Connectivity in High Functioning Autism. *Frontiers in Neurology*, 9:539, July 2018. ISSN 1664-2295. doi:10.3389/fneur.2018.00539. URL https://www.frontiersin.org/article/10.3389/fneur.2018.00539/full.

Brandon A. Zielinski, Molly B. D. Prigge, Jared A. Nielsen, Alyson L. Froehlich, Tracy J. Abildskov, Jeffrey S. Anderson, P. Thomas Fletcher, Kristen M. Zygmunt, Brittany G. Travers, Nicholas Lange, Andrew L. Alexander, Erin D. Bigler, and Janet E. Lainhart. Longitudinal changes in cortical thickness in autism and typical development. *Brain*, 137(6):1799–1812, June 2014. ISSN 1460-2156, 0006-8950. doi:10.1093/brain/awu083. URL https://academic.oup.com/brain/article-lookup/doi/10.1093/brain/awu083.

Jacob Levman, Avilash Das, Allissa MacDonald, Patrick MacDonald, Lindsay Berrigan, and Emi Takahashi. Clinically detectable structural abnormalities in pediatric-onset multiple sclerosis: A large-scale magnetic resonance imaging analysis. *International Journal of Developmental Neuroscience*, 81(2):200–208, April 2021. ISSN 0736-5748, 1873-474X. doi:10.1002/jdn.10090. URL https://onlinelibrary.wiley.com/doi/10.1002/jdn.10090.

Peter A. Brex, Olga Ciccarelli, Jonathon I. O'Riordan, Michael Sailer, Alan J. Thompson, and David H. Miller. A Longitudinal Study of Abnormalities on MRI and Disability from Multiple Sclerosis. *New England Journal of Medicine*, 346(3):158–164, January 2002. ISSN 0028-4793, 1533-4406. doi:10.1056/NEJMoa011341. URL http://www.nejm.org/doi/abs/10.1056/NEJMoa011341.

N. A. Losseff, L. Wang, H. M. Lai, D. S. Yoo, M. L. Gawne-Cain, W. I. McDonald, D. H. Miller, and A. J. Thompson. Progressive cerebral atrophy in multiple sclerosis A serial MRI study. *Brain*, 119(6):2009–2019, 1996. ISSN 0006-8950, 1460-2156. doi:10.1093/brain/119.6.2009. URL https://academic.oup.com/brain/article-lookup/doi/10.1093/brain/119.6.2009.

J.T. Chen, S. Narayanan, D.L. Collins, S.M. Smith, P.M. Matthews, and D.L. Arnold. Relating neocortical pathology to disability progression in multiple sclerosis using MRI. *NeuroImage*, 23(3):1168–1175, November 2004. ISSN 10538119. doi:10.1016/j.neuroimage.2004.07.046. URL https://linkinghub.elsevier.com/retrieve/pii/S1053811904004197.

M. Sailer. Focal thinning of the cerebral cortex in multiple sclerosis. *Brain*, 126(8):1734–1744, June 2003. ISSN 1460-2156. doi:10.1093/brain/awg175. URL https://academic.oup.com/brain/article-lookup/doi/10.1093/brain/awg175.